

Old Dominion University

## ODU Digital Commons

---

Mathematics & Statistics Theses &  
Dissertations

Mathematics & Statistics

---

Winter 1994

### Invariant Manifolds of a Toy Climate Model

Michael Toner

*Old Dominion University*

Follow this and additional works at: [https://digitalcommons.odu.edu/mathstat\\_etds](https://digitalcommons.odu.edu/mathstat_etds)



Part of the [Atmospheric Sciences Commons](#), [Climate Commons](#), [Geophysics and Seismology Commons](#), and the [Mathematics Commons](#)

---

#### Recommended Citation

Toner, Michael. "Invariant Manifolds of a Toy Climate Model" (1994). Doctor of Philosophy (PhD), Dissertation, Mathematics & Statistics, Old Dominion University, DOI: 10.25777/w41a-bm34  
[https://digitalcommons.odu.edu/mathstat\\_etds/63](https://digitalcommons.odu.edu/mathstat_etds/63)

This Dissertation is brought to you for free and open access by the Mathematics & Statistics at ODU Digital Commons. It has been accepted for inclusion in Mathematics & Statistics Theses & Dissertations by an authorized administrator of ODU Digital Commons. For more information, please contact [digitalcommons@odu.edu](mailto:digitalcommons@odu.edu).

# Invariant Manifolds of a Toy Climate Model

by

Michael Toner

B.S., Florida Institute of Technology, 1988

M.S., Old Dominion University, 1990

A Dissertation Submitted to the Faculty of  
Old Dominion University in Partial Fulfillment of the  
Requirements for the Degree of

DOCTOR OF PHILOSOPHY  
Computational and Applied Mathematics

OLD DOMINION UNIVERSITY  
December 5, 1994

Approved by:

\_\_\_\_\_  
A. D. Kirwan Jr. (Director)

\_\_\_\_\_  
John E. Kroll (Co-Director)

\_\_\_\_\_  
  
\_\_\_\_\_

## ABSTRACT

### Invariant Manifolds of a Toy Climate Model

Michael Toner

Old Dominion University, 1994

Director: Dr. A. D. Kirwan Jr.

Co-Director: John E. Kroll

According to astronomical theory, ice ages are caused by variations in the Earth's orbit. However, ice core data shows strong fluctuations in ice volume at a low frequency not significantly present in orbital variations. To understand how this might occur, the dynamics of a two dimensional nonlinear differential equation representing glacier/temperature interaction of an idealized climate was studied. Self sustained oscillation of the autonomous equation was used to model the internal mechanisms that could produce these fluctuations. Periodic parametric modulation of a damped internal oscillation was used to model periodic climate response at double the external modulation period. Both phenomena rely on bounded, structurally stable invariant manifolds that occur when a constant equilibrium solution becomes unstable. For the autonomous formulation, asymptotic analysis was performed to obtain analytic approximations. An outflowing manifold of a second saddle equilibrium formed a heteroclinic connection to the small amplitude periodic orbit of the self sustained oscillation. This connection bifurcated to a homoclinic orbit when the periodic orbit intersected

the saddle equilibrium. For periodic parametric modulations, internal frequencies that give rise to the period doubling phenomena were identified. The Poincaré map showed cases where the bounded outflowing manifold intersects transversally with the unbounded inflowing manifold, a geometry indicative of chaotic dynamics.

Dedicated

to

Renée and Stephen Toner.

## ACKNOWLEDGEMENTS

I would like to thank my friend and mentor Denny Kirwan for undertaking this interdisciplinary project. My committee members Dr. Adam, Dr. Kroll, Dr. Swetits, and Dr. Tweed all gave valuable advice during the final phase.

Special thanks are extended to Dr. Tweed and the Department of Mathematics and Statistics for providing financial support for most of my graduate study. Support during the final phase was provided by the Office of Naval Research through contract N00014-91-1560.

I must also thank Barbara Jeffrey, the secretary of the Department of Mathematics and Statistics. She made my life as a graduate student much easier.

# Contents

List of Figures	vi
<b>1 Formulation</b>	<b>1</b>
1.1 Introduction . . . . .	1
1.2 Formulation . . . . .	7
<b>2 Internal Frequency Analysis</b>	<b>13</b>
2.1 Introduction . . . . .	13
2.2 Maximum $\omega$ for stable periodic orbits . . . . .	16
2.3 Maximum $\omega$ for two equilibria and the heteroclinic connection . . . . .	17
2.4 Minimum $\omega$ and the homoclinic orbit . . . . .	22
2.5 Linear verses nonlinear periods . . . . .	30
2.6 Wave forms as a function of $\omega$ . . . . .	34
<b>3 Periodic Orbital Variation</b>	<b>44</b>
3.1 Introduction . . . . .	44
3.2 The eigenvalues of the monodromy matrix . . . . .	45

3.3	The period doubling effect . . . . .	50
3.4	The geometry of chaos . . . . .	51
<b>4</b>	<b>Conclusions</b>	<b>70</b>
	<b>Bibliography</b>	<b>73</b>
	<b>Appendices</b>	<b>76</b>
<b>A</b>	<b>Chosen Equilibrium</b>	<b>76</b>
<b>B</b>	<b>Complex Eigenvalues and Normal Form</b>	<b>79</b>
<b>C</b>	<b>Poincare-Andronov-Hopf bifurcation</b>	<b>82</b>
<b>D</b>	<b>The Second Equilibrium</b>	<b>86</b>
<b>E</b>	<b>Floquet Theory</b>	<b>91</b>

# List of Figures

2.1	Stability constant $\bar{c}_3(\omega)$ plotted near the maximum stable frequency $\omega_{max} = 2\pi/1055(\text{yr}^{-1})$ . . . . .	18
2.2	Minimum stable period $P_{min}(\text{yr})$ plotted verses equilibrium temperature $T_e(^{\circ}\text{K})$ . . . . .	19
2.3	Periodic orbit in $\mathbf{y}$ coordinates $y_2(^{\circ}\text{K})$ vs $y_1(\text{unitless})$ for the maximum stable frequency $\omega = 2\pi/1055(\text{yr}^{-1})$ . . . . .	20
2.4	Periodic orbit in $\mathbf{u}(\text{yr}^2/^{\circ}\text{K})$ coordinates for $\omega = 2\pi/1055(\text{yr}^{-1})$ . . . . .	21
2.5	Phase trajectory in $\mathbf{y}(\text{yr}^2/^{\circ}\text{K})$ coordinates showing the physical space for $\omega = 2\pi/5700(\text{yr}^{-1})$ . . . . .	23
2.6	Phase trajectory in $\mathbf{u}(\text{yr}^2/^{\circ}\text{K})$ coordinates showing the topology for $\omega = 2\pi/5700(\text{yr}^{-1})$ . . . . .	24
2.7	Maximum period $P_{max}(\text{yr})$ plotted verses equilibrium temperature $T_e(^{\circ}\text{K})$ with $a = 0.1(\text{yr}^2/^{\circ}\text{K})$ . . . . .	26

2.8	Inflowing and outflowing manifolds of the second equilibrium and the periodic orbit about the chosen equilibrium in $\mathbf{u}(\text{yr}^2/^\circ\mathbf{K})$ coordinates for $\omega = 2\pi/20,000(\text{yr}^{-1})$ . The attracting region for the periodic orbit is bounded by the two inflowing manifolds. . . . .	27
2.9	Inflowing and outflowing manifolds of the second equilibrium and the periodic orbit about the chosen equilibrium in $\mathbf{u}(\text{yr}^2/^\circ\mathbf{K})$ coordinates for $\omega = 2\pi/50,000(\text{yr}^{-1})$ . . . . .	28
2.10	Crossing of the inflowing and outflowing manifolds of the second equilibrium in $\mathbf{u}(\text{yr}^2/^\circ\mathbf{K})$ coordinates for $\omega = 2\pi/120,000(\text{yr}^{-1})$ . . . . .	29
2.11	Inflowing and outflowing manifolds in $\mathbf{u}(\text{yr}^2/^\circ\mathbf{K})$ coordinates at the approximate intersection value of $\omega = 2\pi/89277(\text{yr}^{-1})$ . . . . .	31
2.12	The time series $y_2(^\circ\mathbf{K})$ vs $\tau$ ( <i>unitless</i> ) of the saddle manifolds for $\omega = 2\pi/89277(\text{yr}^{-1})$ . The periodic orbit bifurcating from the homoclinic orbit attracts in negative time. . . . .	32
2.13	The time series $y_2(^\circ\mathbf{K})$ vs $\tau$ ( <i>unitless</i> ) of the saddle manifolds for $\omega = 2\pi/89276(\text{yr}^{-1})$ . The periodic orbit bifurcating from the homoclinic orbit attracts in positive time. . . . .	33
2.14	Geometric sketch of the Poincaré map for a two dimensional phase trajectory. . . . .	35

2.15	Period ( $\text{yr}$ ) of the periodic orbit plotted versus $2\pi/\omega(\text{yr})$ . Solutions near the equilibrium (inside the periodic orbit) will rotate at the rate of $2\pi/\omega(\text{yr})$ initially. However, at $t \rightarrow \infty$ , the rotation rate slows to the given period value as it approaches the periodic orbit. . . . .	36
2.16	Maximum temperature deviation from equilibrium $T_{max} (^{\circ}\text{K})$ plotted from $P_{min}(\text{yr})$ to $P_{max}(\text{yr})$ with $T_e = 246 (^{\circ}\text{K})$ and $a = 0.1 (\text{yr}^2/^{\circ}\text{K})$ .	38
2.17	Maximum glaciation deviation from equilibrium $G_{max}$ plotted from $P_{min}(\text{yr})$ to $P_{max}(\text{yr})$ with $T_e = 246 (^{\circ}\text{K})$ and $a = 0.1 (\text{yr}^2/^{\circ}\text{K})$ . . .	39
2.18	Wave forms in glaciation for $\omega_1 = 2\pi/70,000(\text{yr}^{-1})$ (top wave), $\omega_2 = 2\pi/79,600(\text{yr}^{-1})$ (middle wave), and $\omega_3 = 2\pi/89,200(\text{yr}^{-1})$ (bottom wave) with $T_e = 246 (^{\circ}\text{K})$ and $a = 0.1 (\text{yr}^2/^{\circ}\text{K})$ . . . . .	41
2.19	Wave forms in temperature for $\omega_1 = 2\pi/70,000(\text{yr}^{-1})$ (bottom wave), $\omega_2 = 2\pi/79,600(\text{yr}^{-1})$ (middle wave), and $\omega_3 = 2\pi/89,200(\text{yr}^{-1})$ (top wave) with $T_e = 246 (^{\circ}\text{K})$ and $a = 0.1 (\text{yr}^2/^{\circ}\text{K})$ . . . . .	42
2.20	Phase trajectory in $\mathbf{y}$ for the maximum and minimum $\omega$ values $\omega_{max} = 2\pi/1055(\text{yr}^{-1})$ and $\omega_{min} \simeq 2\pi/89,200(\text{yr}^{-1})$ with $T_e = 246 (^{\circ}\text{K})$ and $a = 0.1 (\text{yr}^2/^{\circ}\text{K})$ . . . . .	43
3.1	The eigenvalues $\gamma_{1,2}(\omega, \delta)$ for $\omega = 2\pi/20,000(\text{yr}^{-1})$ plotted against $\delta/B$ . . . . .	53
3.2	Real and imaginary parts of $\gamma_{1,2}(\omega, \delta)$ for $\omega = 2\pi/21,000(\text{yr}^{-1})$ plotted against $\delta/B$ . . . . .	54

3.3	Real and imaginary parts of $\gamma_{1,2}(\omega, \delta)$ for $\omega = 2\pi/18,000(\text{yr}^{-1})$ plotted against $\delta/B$ . . . . .	55
3.4	Real and imaginary parts of $\gamma_{1,2}(\omega, \delta)$ for $\omega = 2\pi/16,000(\text{yr}^{-1})$ plotted against $\delta/B$ . . . . .	56
3.5	Real and imaginary parts of $\gamma_{1,2}(\omega, \delta)$ for $\omega = 2\pi/12,500(\text{yr}^{-1})$ plotted against $\delta/B$ . . . . .	57
3.6	Real and imaginary parts of $\gamma_{1,2}(\omega, \delta)$ for $\omega = 2\pi/26,666(\text{yr}^{-1})$ plotted against $\delta/B$ . . . . .	58
3.7	Generic mapping for a saddle type linear map with two positive eigenvalues. . . . .	59
3.8	Generic mapping for a saddle type linear map with two negative eigenvalues. . . . .	60
3.9	Double period fixed points (top) and outflowing manifolds (bottom) in $\mathbf{u}$ coordinates for $\omega = 2\pi/12,500(\text{yr}^{-1})$ and $\delta/B = 0.0076$ . . . . .	61
3.10	Double period wave forms in $\mathbf{y}$ coordinates for $\omega = 2\pi/12,500(\text{yr}^{-1})$ and $\delta/B = 0.0076$ . . . . .	62
3.11	Double period fixed points (top) and outflowing manifolds (bottom) in $\mathbf{u}$ coordinates for $\omega = 2\pi/26,666(\text{yr}^{-1})$ and $\delta/B = 0.00272$ . . . . .	63
3.12	Double period wave forms in $\mathbf{y}$ coordinates for $\omega = 2\pi/26,666(\text{yr}^{-1})$ and $\delta/B = 0.00272$ . . . . .	64
3.13	Inflowing and outflowing manifolds for the nonchaotic parameters $\omega = 2\pi/12,500(\text{yr}^{-1})$ and $\delta/B = 0.0076$ . . . . .	65

3.14 Inflowing and outflowing manifolds for the chaotic parameters $\omega = 2\pi/12,500(\text{yr}^{-1})$ and $\delta/B = 0.0084$ . . . . .	66
3.15 Time series for $y_1 = G - G_e$ of four initial conditions along unstable manifold for the nonchaotic parameters $\omega = 2\pi/12,500(\text{yr}^{-1})$ and $\delta/B = 0.0076$ . The two solutions initially in phase (top) on either side of the equilibrium coalesce (bottom) after 100 iterations of the Poincaré map. . . . .	67
3.16 Time series for $y_1 = G - G_e$ of four initial conditions along unstable manifold for the chaotic parameters $\omega = 2\pi/12,500(\text{yr}^{-1})$ and $\delta/B = 0.0084$ . The two solutions initially in phase (top) on either side of the equilibrium remain in phase (bottom) after 20 iterations of the Poincaré map. . . . .	68
3.17 Time series for $y_1 = G - G_e$ of four initial conditions along unstable manifold for the chaotic parameters $\omega = 2\pi/12,500(\text{yr}^{-1})$ and $\delta/B = 0.0084$ after 50 iterations (top) and 100 iterations (bottom) of the Poincaré map. . . . .	69

# Chapter 1

## Formulation

### 1.1 Introduction

Since the pioneering work of Lorenz in the early 1960's [9] toy models have played an important role in both geophysics and dynamical systems. Toy climate models, for example, have been used as "sanity checks" for the results from primitive equation based climate simulations [4].

Climate models fall in to two main categories [8]: equilibrium models and differential models. Equilibrium models presume the climate is near equilibrium at all times and any change in the parameters of the planet results in a slow adjustment of the equilibrium. Differential models presume the climate is in motion and any change in the parameters varies this motion. Stable equilibrium solutions of differential models can give rise to simple equilibrium models.

A primary issue in climate dynamics [4] is to relate the surface albedo of the Earth

to the global temperature. Of course the exact relationship between the two, if one exists, is impossible to obtain. Thus, for practical reasons, we are forced to use small dimensional or toy climate models to relate gross aspects of the temperature to the albedo.

According to the astronomical theory of ice ages developed by Milankovitch [10], the Earth's orbital variation causes cycles in the average radiation received from the Sun, thus contributing to the growth and recession of glaciers. However, very little orbital variation exists at the 100,000 year period although this period dominates climate data for the last 600,000 years [14],[8]. Dominant orbital variation exists at 20,000 year and 40,000 year periods; thus internal mechanisms are believed to be responsible for the 100,000 year periodicity. This notion is supported by the fact that climate records longer than 600,000 years do not exhibit the strong 100,000 year cycle [8].

Clearly, an equilibrium model cannot explain the 100,000 year internal cycle. The mechanisms that contribute to this internal feedback are not obvious. Both deterministic and statistical approaches have been utilized to approximate these internal mechanisms using differential models.

The models used by Nicolis and Nicolis [11] and Benzi et al. [1] use random forcing of a nonlinear energy balance differential equation governing temperature. Both models show two stable equilibrium temperatures separated by an unstable equilibrium. The random forcing term in both cases moves the temperature between the two stable temperatures. Nicolis and Nicolis use the Fokker-Planck equation with

piecewise linear variation of albedo with temperature. Benzi et al. directly impose three equilibria with the form of their equation, do not incorporate albedo effects and introduce 100,000 year periodicity.

Deterministic models include explicit mechanisms believed to be important in climate dynamics. Clearly, a system of linear differential equations cannot support structurally stable periodic motion without external forcing at the prescribed period. This limitation can be overcome with a nonlinear system. Nonlinear systems of differential equations exhibit a rich variety of behavior and allow plausible physical mechanisms missing from linear systems. Solutions comprising the invariant manifolds in the phase space of the equations give the local topology, showing how these mechanisms effect the dynamics.

North [12] studied the relationship between the solar constant and the latitude of the ice sheet edge between glaciated and unglaciated surface. A linear empirical formula for infrared flux in terms of temperature was utilized. Thermal diffusion was used for the energy balance equation to form a linear differential equation. By implicitly defining the location of the ice sheet edge, the system became nonlinear. Analytic approximations in terms of hypergeometric functions showed two stable equilibrium latitudes (one corresponding to the present climate and one corresponding to an ice covered Earth) separated by an unstable equilibrium latitude. The results show that a small drop in the solar constant could move the present stable climate to an ice covered Earth.

Ghil and Tavantzis [5] utilized a piecewise linear radiation balance equation cou-

pled to a nonlinear mass balance equation for the ice sheets. The assumptions on the ice sheets give a parabolic profile of the glaciers. Phase space analysis of the two autonomous differential equations showed a stable limit cycle about a constant (unstable) equilibrium and two saddle type equilibria. The limit cycle supported internal oscillation at the 100,000 year period. The two saddle equilibria as well as the stability constant for the limit cycle were determined numerically. A homoclinic orbit bifurcating from the limit cycle was shown to exist when an inflowing and an outflowing manifold of one of the saddle equilibria intersected. Also shown to exist was a heteroclinic connection between the two saddle equilibria while the limit cycle was still present.

The differential climate model developed by Posmentier [14] is particularly interesting. This two dimensional model couples a logistic growth law for uniform depth glacier advancement with a nonlinear energy balance equation. A constant equilibrium is assumed, and the dynamical equations are shifted to this equilibrium to form deviation equations. Periodic parametric perturbations of these deviation equations represent the effects of orbital variations. Posmentier reported periodic, quasiperiodic, and chaotic solutions but did not show how these solutions arise; nor did he examine the global behavior of the autonomous equations as did Ghil and Tavantzis [5].

The elegant formulation and the robust behavior of this model make it appealing. We present a thorough analysis using techniques of dynamical systems theory. In

particular, invariant manifold structures that can provide low frequencies not present in orbital variation will be examined. Also, the question of how chaotic dynamics can occur will be addressed by studying these invariant manifolds.

Since both stable and unstable constant equilibrium solutions have been proposed, we will examine both. For the autonomous system, we obtain a phase portrait similar to the model used by Ghil and Tavantzis [5]. However, we provide an analytic stability constant for the limit cycle, an asymptotic approximation of a second equilibrium, and an asymptotic approximation of when the limit cycle bifurcates to a homoclinic orbit. Periodic parametric perturbations of the stable equilibrium solution is examined using Floquet theory. A combination of simple analytic analysis and numerical computation of the monodromy matrix allows us to determine how the equilibrium becomes unstable, and the type of structure that bifurcates from it.

One of the most important characteristics of nonlinear systems is that they provide bounded behavior when the linearized version becomes unbounded. For example the scalar logistic growth model  $\dot{x} = kx - \lambda x^2$ , when linearized about  $x = 0$ , becomes the exponential growth model  $\dot{x} = kx$ . The bounded behavior of the logistic model is due exclusively to the nonlinear term  $\lambda x^2$  that provides the second equilibrium  $x = k/\lambda$ .

In the periodic orbits of the the Poincaré-Andronov-Hopf bifurcation, which occur in two (and higher) dimensions, the nonlinear terms bound the outward radial component of spiral source equilibria for differential equations. Nonlinear terms also can bound the outflowing manifolds of equilibria for two dimensional maps via saddle node bifurcation. Both of these invariant manifold structures are utilized in studying

Posmentier's model.

However, the same tendency that keeps linearly unstable motion bounded also can cause chaotic dynamics. Chaotic dynamics are associated with intersecting saddle manifolds where stretching and contracting occur in the phase space [16], [17]. Geometry is the key factor in chaotic dynamics. The Smale Horseshoe, for example, is a piecewise linear map that has a chaotic invariant set due to the geometry of the mapping. Although this map was contrived to produce such a set, it does give a good indication of what goes on when certain geometrical conditions are met.

Often chaotic motion is declared to be present after a series of numerical experiments calculating quantities such as Liapunov exponents or fractal dimension [13]. This technique has been applied with varying success to both data and model output. With this approach one cannot predict the onset of chaos, but merely suggest that it is present. We will determine when chaos can occur by studying the inflowing and outflowing manifolds of the Poincaré map for the periodic parametric modulation.

Since the assumptions made in the formulation do not include such realistic features as an atmosphere and ocean, variations in albedo, or vegetation we do not expect the model to reproduce geological data. There are many quantitative models, some of them quite large, that match some aspects of geological data. Instead, our focus is to understand the role of the nonlinear feedback mechanisms present in such models and how different modes of behavior can arise.

There has not been extensive application of dynamical systems techniques to climatology. Consequently, we hope the results presented here will prove useful and

significant in assessing other model performance.

## 1.2 Formulation

The modified logistic growth equation for a planetary glacier coupled with an energy balance equation for the planet takes the following form:

$$\begin{aligned}\dot{G} &= RG(1 - G) - AG - BT + C \\ \dot{T} &= L\dot{G} - KT^4 + F(1 - G).\end{aligned}\tag{1.2.1}$$

Here  $G$  is the fraction of the planet surface covered by glaciation and  $T$  is the average radiation temperature of the planet. Although the model does not account for geographic variability or the presence of an ocean it does account for a number of physical processes that are believed to be important in climate fluctuations. This model was first introduced by Posmentier [14].

In the equation for  $\dot{T}$ , the first term  $L\dot{G}$  accounts for warming associated with latent heat released by growth of the glacier. The parameter  $L$  is proportional to the latent heat of evaporation. The long-wave black body radiation leaving the planet is accounted for by  $KT^4$  with  $K$  being proportional to the black-body emissivity. Absorption of short-wave radiation by the non-glaciated portion of the planet is represented by  $F(1 - G)$  with  $F$  being proportional to the albedo of the bare planet surface.

The first term in the function for  $\dot{G}$  accounts for the portion of the total planetary evaporation that falls on the glacier, thus contributing to its growth. The parameter  $R$

is proportional to the evaporation rate. The  $AG$  term accounts for enhanced melting when the glacier grows and advances towards the equator. Next,  $BT$  accounts for the balance between enhanced melting and increased precipitation when the temperature rises. For  $B > 0$  the melting dominates and  $B < 0$  the precipitation dominates. Finally,  $C$  is used as a planetary constant. The parameters  $A, B, C$  are considered soft since values can not be readily prescribed. We use them to tune the model.

The parameter  $C$  is chosen to obtain a constant equilibrium at  $T = T_e$  and  $G = 1 - \kappa T_e^4$  where  $K = \kappa F$  and  $T_e$  is a chosen temperature. Details are described in Appendix A. The equilibrium glaciation value is adjusted with the parameter  $\kappa$ .

We begin by translating this equilibrium to the origin. Let

$$G = y_1 + 1 - \kappa T_e^4 \quad (1.2.2)$$

$$T = y_2 + T_e. \quad (1.2.3)$$

Equations (1.2.1) with  $C$  given by (A.5) then become

$$\dot{\mathbf{y}} = \mathbf{A} \mathbf{y} + \mathbf{f}(\mathbf{y}) \quad (1.2.4)$$

where  $\mathbf{y} = \begin{bmatrix} y_1 \\ y_2 \end{bmatrix}$ ,

$$\mathbf{A} = \begin{bmatrix} 2R\kappa T_e^4 - R - A & -B \\ 2LR\kappa T_e^4 - LR - LA - F & -LB - 4\kappa FT_e^3 \end{bmatrix} \quad (1.2.5)$$

and

$$\mathbf{f}(\mathbf{y}) = \begin{bmatrix} Ry_1^2 \\ LRy_1^2 + \kappa Fy_2^4 + 4\kappa Fy_2^3T_e + 6\kappa Fy_2^2T_e^2 \end{bmatrix}. \quad (1.2.6)$$

The equations (1.2.4) are called the deviation equations.

The parameters  $A$  and  $B$  are used to prescribe the eigenvalues of  $\mathbf{A}$ . Details are given in Appendix B.

In (1.2.4) the linearized flow ( $\mathbf{f} = \mathbf{0}$ ) is topologically governed by the eigenvalues of the coefficient matrix  $\mathbf{A}$ . If the eigenvalues are of the form  $\alpha \pm i\omega$ , then for  $\omega \neq 0$ , all solutions will spiral toward zero for  $\alpha < 0$ , spiral away from zero for  $\alpha > 0$ , or form a periodic orbit about zero for  $\alpha = 0$  with a rotation period of  $2\pi/\omega$ .

Clearly, the periodic orbits of the linear system are structurally unstable. The nonlinear flow of (1.2.4) is much more interesting since a structurally stable periodic orbit can exist for  $\alpha > 0$  through Poincaré-Andronov-Hopf bifurcation. This phenomenon is often referred to as self sustained oscillation since no external mechanism is needed to obtain this periodic orbit.

The required values for  $A$  and  $B$  that provide eigenvalues of this type are given by (B.2). The equation for  $B$  in (B.2) shows that for  $\alpha > 0$ ,  $B < 0$ . Since the self sustained oscillation requires  $\alpha > 0$ , this provides an interpretation of the balance between enhanced melting and increased precipitation when the temperature rises; the increased precipitation effect must dominate enhanced melting as the glacier grows.

To study the internal mechanisms associated with self sustained oscillation, we consider an autonomous formulation. The bifurcation technique employed requires the radial motion (governed by  $\alpha$ ) to be small compared to the rotational motion (governed by  $\omega$ ). Emphasizing this, we let  $\alpha = \lambda\omega$  and consider  $0 < \lambda \ll 1$ .

The small amplitude periodic orbit is given by

$$\mathbf{y}(t) = a\mathbf{P} \begin{bmatrix} \cos \theta(t) \\ -\sin \theta(t) \end{bmatrix} + O(a^3)$$

where the matrix  $\mathbf{P}$  defined in (B.6) puts  $\mathbf{A}$  in Jordan Form,  $a$  is the approximate amplitude of the orbit in the coordinates  $\mathbf{u} = \mathbf{P}^{-1}\mathbf{y}$ , and  $\theta(t)$  parameterizes the orbit. Details are given in Appendix C. The bifurcation curve relating  $\lambda$  with the radius  $a$  is given by  $\lambda(a) = -\bar{c}_3 a^2 + O(a^3)$ ,  $a \rightarrow 0$  where the constant  $\bar{c}_3$  determines the stability of the resulting periodic orbit. For parameter values such that  $\bar{c}_3 < 0$  stable periodic orbits exist. An analytic expression of  $\bar{c}_3$  is given in (C.10).

To study further properties of the phase space for low frequency self sustained oscillations, we consider  $\omega$  also as a small expansion parameter. Using arguments presented in Appendix D when  $\omega = \alpha = 0$  it is shown that a double root exists at  $\mathbf{y} = \mathbf{0}$ . For  $\omega$  small a second equilibrium is  $O(\omega^2)$  close to the chosen equilibrium. The eigenvalues of the system linearized about this second equilibrium are  $\pm\omega + O(\omega^2) + O(\frac{\alpha^2}{\omega^2})$ . Therefore the topology we study for the autonomous formulation is that of a periodic orbit at  $\mathbf{y} = \mathbf{0}$  with a nearby saddle at  $\mathbf{y} = \mathbf{y}_{\text{saddle}}$ .

To consider the question of external influence on the idealized planet in question, we will study the effect of a single frequency periodic perturbation to the deviation equations. As discussed in [14] and [8], the Earth's orbital parameters have strong 20,000 year variation due to precession, a weaker 40,000 year variation due to obliquity, and an even weaker 100,000 year variation due to ellipticity variations. Posmentier [14] analyzed the response of the model to the dominant 20,000 year vari-

ation by replacing the parameter  $B$  in (1.2.4) by the term  $B(1 + S \cos \sigma t)$  where  $\sigma = 2\pi/20,000(\text{yr}^{-1})$ . A wide variety of behavior was reported, including solutions that appeared to be chaotic.

With this perturbation, the equations (1.2.4) become

$$\dot{\mathbf{y}} = \hat{\mathbf{A}}(\sigma t, \delta) \mathbf{y} + \mathbf{f}(\mathbf{y}) \quad (1.2.7)$$

where

$$\hat{\mathbf{A}}(\sigma t, \delta) = \mathbf{A} + \delta \cos \sigma t \begin{bmatrix} 0 & -1 \\ 0 & L \end{bmatrix} \quad (1.2.8)$$

and  $\delta = BS$ . Since  $\hat{\mathbf{A}}(\sigma t)$  is periodic and (1.2.7) is homogeneous, the natural tool of analysis is the Floquet representation for the linearized Poincaré map. This technique is described in Appendix E. The eigenvalues of this linearized Poincaré map give local behavior of the nonlinear system near  $\mathbf{y} = \mathbf{0}$ .

The two dimensional nonlinear Poincaré map can undergo a Poincaré-Andronov-Hopf bifurcation similar to two dimensional nonlinear autonomous differential equations. However the resulting torus that is formed contains only the internal and external frequencies. The physics of this behavior still relies on the self sustained oscillation.

To study different phenomena, we consider how lower frequencies can be introduced internally without relying on the self sustained oscillation. These frequencies come about through saddle node bifurcation and a phenomenon called period doubling. The period doubled is that of the external modulation.

Physically, we consider the internal response to be that of damped oscillatory motion with a frequency near the modulation frequency. Thus, eigenvalues of the matrix  $\mathbf{A}$  are set to  $\alpha \pm i\omega$  with  $\alpha < 0$ . We will assume that the internal damping (governed by  $\alpha$ ) is small compared to the internal rotation rate (governed by  $\omega$ ), although the technique employed does not require this. For uniformity we will let  $\alpha = \lambda\omega$  and consider  $-1 \ll \lambda < 0$ .

We use simple analytic analysis to determine possible  $\omega$  values that could support the period doubling phenomenon. Both cases of subexternal and superexternal planetary response to the modulation are examined. A numerical bifurcation curve for the eigenvalues of the monodromy matrix determines specific  $(\delta, \omega)$  values needed. The eigenvalues of this matrix are the same as the eigenvalues of the linearized Poincaré map.

Using the eigenvectors of the monodromy matrix for initial conditions, we then examine the saddle manifolds of the nonlinear Poincaré map. Period doubling typically occurs when the outflowing manifolds remain bounded.

If the inflowing and outflowing manifolds of a two dimensional map intersect transversally, then the typical response is the generation of a chaotic invariant set. This intersection provides the generation of a transversal homoclinic point. It is rare to be able to establish theoretically the existence of such a point [7]. Generally, numerical evidence must be used.

# Chapter 2

## Internal Frequency Analysis

### 2.1 Introduction

The unperturbed equations 1.2.4 have several types of invariant manifolds. There are two equilibria, one of which is either a spiral sink or source. The other equilibrium is a saddle. When the spiral equilibrium is a source, we have the additional invariant set of a periodic orbit. Emanating from the saddle are four invariant manifolds: two inflowing manifolds and two outflowing manifolds. What is the relationship between the two equilibria? What, if any effect does one have on the other? Are there trajectories linking the two and what does the local phase space look like? What is the difference between the linear frequency and the frequency of the nonlinear equations?

We will use a combination of the asymptotic analysis and numerical integration to answer these questions. Of primary focus, we will consider the rotation rate  $\omega$  of

the linear system near the chosen equilibrium. Our approach here will be to fix the radius of the periodic orbit and consider how the system changes as a function of the frequency.

There are two classes of parameters to be treated here: soft and fixed. Although by no means is the distinction clear as to the class in which a particular parameter is in, for the purposes of this chapter, we will treat the frequency  $\omega$  as the most flexible parameter. The equilibrium radiation temperature will mostly be taken to be  $T_e = 246(^{\circ}\mathbf{K})$  as in [14], although certain bifurcation values of  $\omega$  will be plotted for a range of  $T_e$ .

For the parameters considered as fixed, we will use the values given by [14]

$$\begin{aligned}
 L &= 20 (^{\circ}\mathbf{K}) \\
 K &= 1.07 * 10^{-10} \left(\frac{1}{^{\circ}\mathbf{K} \mathbf{yr}}\right) \\
 F &= .43395 \left(\frac{^{\circ}\mathbf{K}}{\mathbf{yr}}\right) \\
 R &= 8 * 10^{-5} \left(\frac{1}{\mathbf{yr}}\right). \tag{2.1.1}
 \end{aligned}$$

The units of  $A$  and  $C$  are  $(1/\mathbf{yr})$ , the units of  $B$  are  $(^{\circ}\mathbf{K}^{-1} \mathbf{yr}^{-1})$ , and the units of  $\alpha$  and  $\omega$  are  $\mathbf{yr}^{-1}$ . Both components of the vector  $\mathbf{u}$  and the radius  $a$  are in units of  $(\mathbf{yr}^2/^{\circ}\mathbf{K})$ . Time will be scaled by  $\tau = \omega t$ . For notational convenience we will write  $G_e = 1 - \kappa T_e^4$ .

The parameter  $a$  gives the most direct control of the magnitude of the periodic orbit. Although the assumption that  $a \rightarrow 0$  places an inherent restriction on the radius of the periodic orbit, this “near equilibrium” analysis is useful in determining

parameter interplay. We will set  $a = 0.1 \text{ (yr}^2/\text{°K)}$  for the experiments to show the general trend of the model.

Certainly quantitatively different results can be obtained by examining a wider range of parameter values. However, we expect the qualitative behavior to be the same.

Integrations are done (in  $y$  coordinates) with the LSODA routine of the public domain software ODEPACK using initial conditions from Maple. Initial conditions for the periodic orbits are obtained using asymptotic analysis resulting from the Poincaré-Andronov-Hopf bifurcation described in Appendix C. The saddle manifolds of the second equilibrium are determined by first locating the equilibrium numerically and then calculating the eigenvalues and eigenvectors of the matrix (D.7) at the determined equilibrium. Then the outflowing manifolds are integrated in positive time using small ( $10^{-5}$  to  $10^{-9}$ ) displacements from the second equilibrium in the direction of the eigenvectors corresponding to the positive eigenvalue. The inflowing manifolds are integrated in negative time along the eigenvectors corresponding to the negative eigenvalue. Trajectories integrated in positive time are solid lines, while dashed lines correspond to trajectories integrated in negative time. Arrows indicate the direction of the flow for positive time.

Several types of invariant sets are obtained in this chapter. For higher frequencies, one outflowing manifold forms a heteroclinic orbit connecting the saddle equilibrium to either the spiral sink (for  $\alpha < 0$ ) or the periodic orbit about the spiral source (for  $0 < \alpha \ll 1$ ). In studying the periodic orbits for lower frequencies, we find the

additional invariant set of a homoclinic orbit that occurs when an inflowing and an outflowing manifold cross. Some of these results are given in [15].

## 2.2 Maximum $\omega$ for stable periodic orbits

Recall that the stability of the periodic orbit depends upon the sign of the constant  $\bar{c}_3$  defined in (C.10). Treating  $\bar{c}_3$  as a function of  $\omega$  we can determine what ranges of  $\omega$  give rise to stable ( $\bar{c}_3 < 0$ ) and unstable periodic orbits. The stability of the periodic orbit is independent of the radius  $a \ll 1$ .

We set  $T_e = 246(^{\circ}\text{K})$  and plot  $\bar{c}_3$  in Fig. 2.1. The maximum  $\omega$  value for stability can be determined by locating the value  $\omega = \omega_{max}$  such that  $\bar{c}_3(\omega_{max}) = 0$ . From (C.10), we see that  $\bar{c}_3 = 0$  only at the roots of the quadratic in  $\omega^2$

$$\begin{aligned}
& 3L^2(10L\kappa FT_e^3 + T_e R + F)\omega^4 + \\
& (48L^2F^2\kappa^2T_e^7R - 72L^2F^3\kappa^2T_e^6 + 8LF\kappa T_e^5R^2 - \\
& 12LF^2\kappa T_e^4R + 30LF^3\kappa T_e^3 + 2FT_e^2R^2 + 3F^3)\omega^2 \\
& + 8\kappa^2T_e^6F^3(2T_eR - 3F)(8LR\kappa T_e^4 + 2T_eR + 3F) \\
& = 0.
\end{aligned} \tag{2.2.2}$$

The maximum value of  $\omega$  that produces a stable periodic orbit is then

$$\begin{aligned}
\omega_{max}^2 = & \frac{1}{60\kappa FT_e^3L^3 + 6L^2RT_e + 6L^2F} \{-3F^3 \\
& - 48L^2\kappa^2T_e^7RF^2 + 72L^2\kappa^2F^3T_e^6 - 8LR^2\kappa T_e^5F
\end{aligned}$$

$$\begin{aligned}
& +12 LR\kappa T_e^4 F^2 - 30 L\kappa F^3 T_e^3 - 2 R^2 F T_e^2 \\
& + F(1 + 4\kappa T_e^3 L) ( 816 L^2 \kappa^2 F^2 R^2 T_e^8 \\
& - 1008 L^2 \kappa^2 R F^3 T_e^7 - 324 L^2 \kappa^2 F^4 T_e^6 \\
& + 48 LR^3 \kappa F T_e^6 - 72 L\kappa F^2 R^2 T_e^5 \\
& + 72 LR\kappa F^3 T_e^4 - 4 R^4 T_e^4 - 108 L\kappa F^4 T_e^3 \\
& - 12 R^2 F^2 T_e^2 - 9 F^4 )^{1/2} \}. \tag{2.2.3}
\end{aligned}$$

Plotting  $P_{min} = 2\pi/\omega_{max}$  versus  $T_e$  in Fig. 2.2 we obtain minimum stable periods as a function of the chosen equilibrium temperature. Notice that this minimum period is independent of the radius  $a$ .

In Fig. 2.3 the periodic orbit is shown in  $y$  coordinates for the maximum stable frequency  $\omega = 2\pi/1055(\text{yr}^{-1})$ . The same orbit in  $u$  coordinates is shown in Fig. 2.4.

### 2.3 Maximum $\omega$ for two equilibria and the heteroclinic connection

We have set an equilibrium temperature and hence an equilibrium glaciation is obtained by (C.10) with  $T = T_e$ . However, care needs to be taken when examining the dynamics of the second equilibrium because it may not lie in physical space. The approximation of this second equilibrium in (D.6) allows us to estimate when two equilibria lie in physical space. Since the glaciation must be between 0 and 1, we can

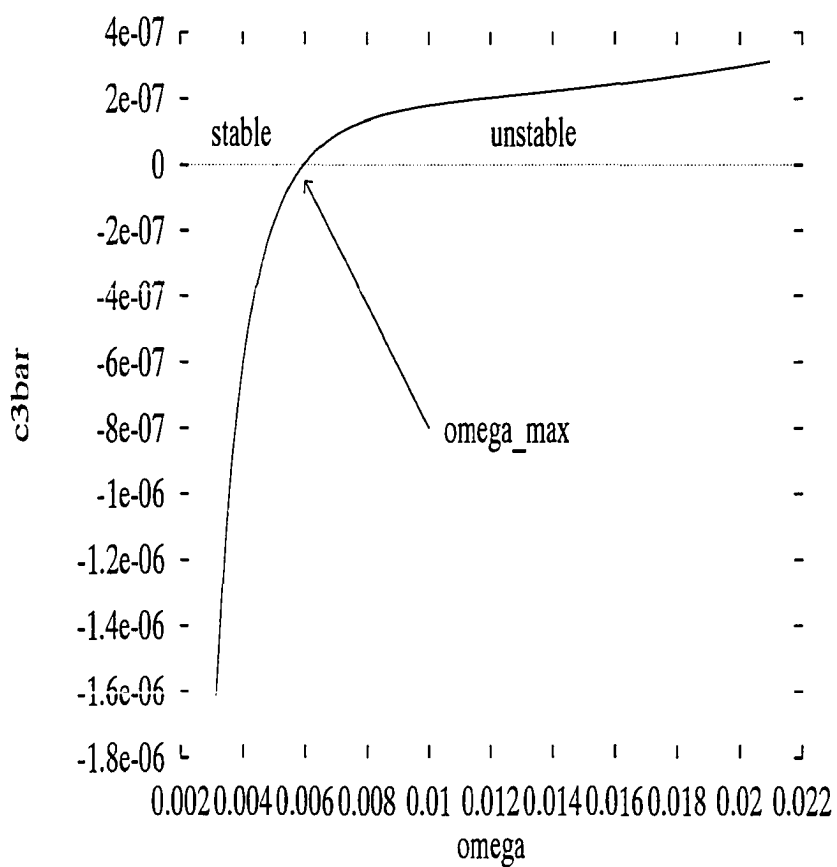


Figure 2.1: Stability constant  $\bar{c}_3(\omega)$  plotted near the maximum stable frequency

$$\omega_{max} = 2\pi/1055(\text{yr}^{-1})$$

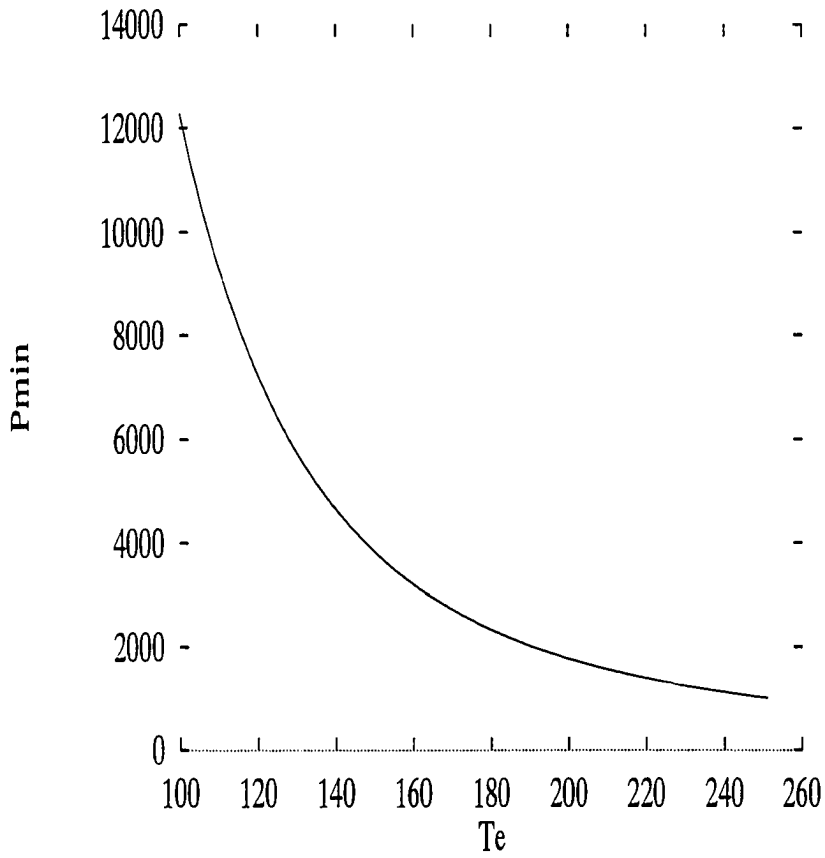


Figure 2.2: Minimum stable period  $P_{min}$  (yr) plotted versus equilibrium temperature  $T_e$  (°K).

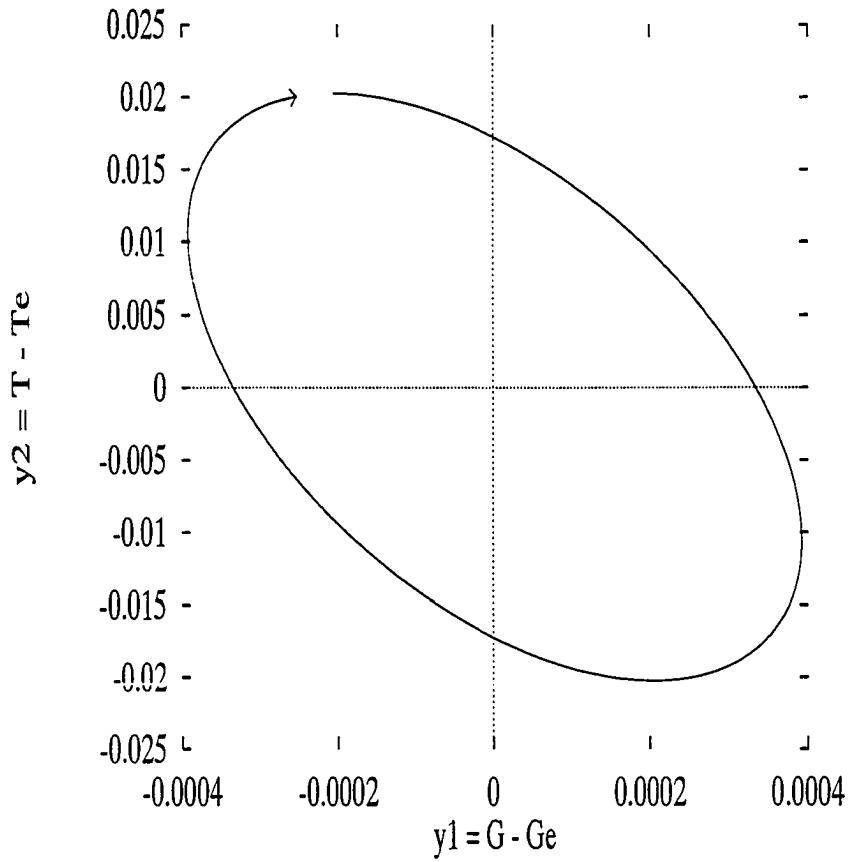


Figure 2.3: Periodic orbit in  $y$  coordinates  $y_2$  ( $^{\circ}\mathbf{K}$ ) vs  $y_1$  (*unitless*) for the maximum stable frequency  $\omega = 2\pi/1055(\mathbf{yr}^{-1})$ .

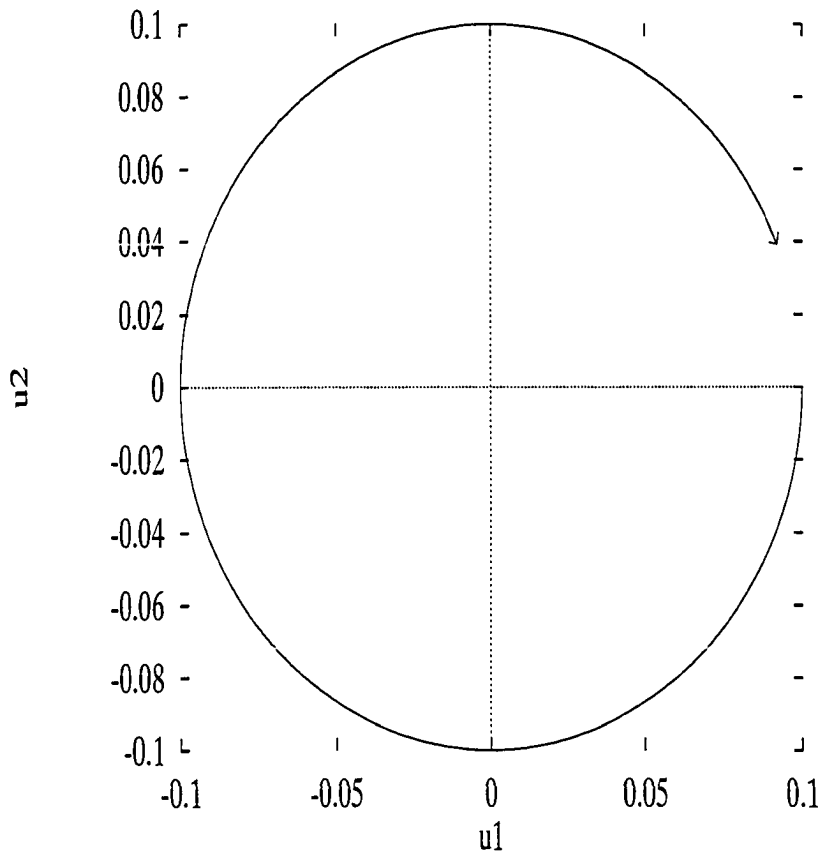


Figure 2.4: Periodic orbit in  $u$  ( $\text{yr}^2/^\circ\text{K}$ ) coordinates for  $\omega = 2\pi/1055(\text{yr}^{-1})$ .

solve

$$G_2 = -\frac{(1 + 4\kappa T_e^3 L)\omega^2}{2\kappa T_e^2(2RT_e + 8LR\kappa T_e^4 + 3F)F} + \frac{3\kappa F^4 T_e^2(-2RT_e + 3F)a^2}{2RT_e + 8LR\kappa T_e^4 + 3F} + 1 - \kappa T_e^4 \quad (2.3.4)$$

for  $G_2 = 1$  and  $G_2 = 0$  in terms of  $\omega$ .

Examining (2.3.4), we see that for real  $\omega$  values,  $G_2 \neq 1$ . Thus we are left to examine where  $G_2 > 0$ . Doing this yields

$$\omega_{2eq}^2 = -\frac{6\kappa^2 T_e^4 F^5 (2RT_e - 3F)a^2}{1 + 4\kappa T_e^3 L} - \frac{2\kappa T_e^2 (2RT_e + 8LR\kappa T_e^4 + 3F)F(\kappa T_e^4 - 1)}{1 + 4\kappa T_e^3 L} \quad (2.3.5)$$

For the parameters selected, we have  $\omega_{2eq} = 2\pi/5482(\text{yr}^{-1})$ . However, this is based upon an asymptotic approximation for the second equilibrium. Using a numerical root finder, we see that this value is still too large.

We examine the phase portrait of the system for  $\omega = 2\pi/5700(\text{yr}^{-1})$ . In Fig. 2.5 the  $y$  coordinates are shown with the boundaries of the physical space. Figure 2.6 allows the topological aspect of the local phase space to be discerned.

## 2.4 Minimum $\omega$ and the homoclinic orbit

If the periodic orbit intersects the second equilibrium we expect a bifurcation to occur. So we may obtain a minimum frequency  $\omega_{min}$  of the periodic orbit in terms of  $a$  by using  $u$  coordinates, since the orbit in this coordinate system is a circle. This intersection is determined by solving the equation

$$a = \left\| \mathbf{P}^{-1}(y_{saddle}) \right\|_{\mathbf{u}} \quad (2.4.6)$$

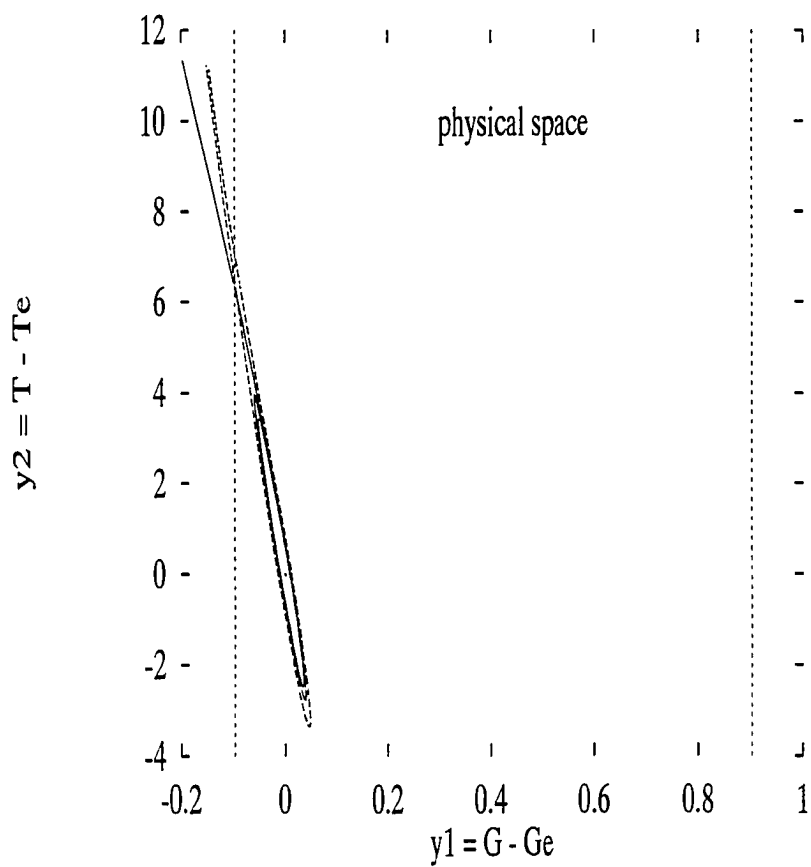


Figure 2.5: Phase trajectory in  $y$  ( $\text{yr}^2/\text{°K}$ ) coordinates showing the physical space for  $\omega = 2\pi/5700(\text{yr}^{-1})$ .

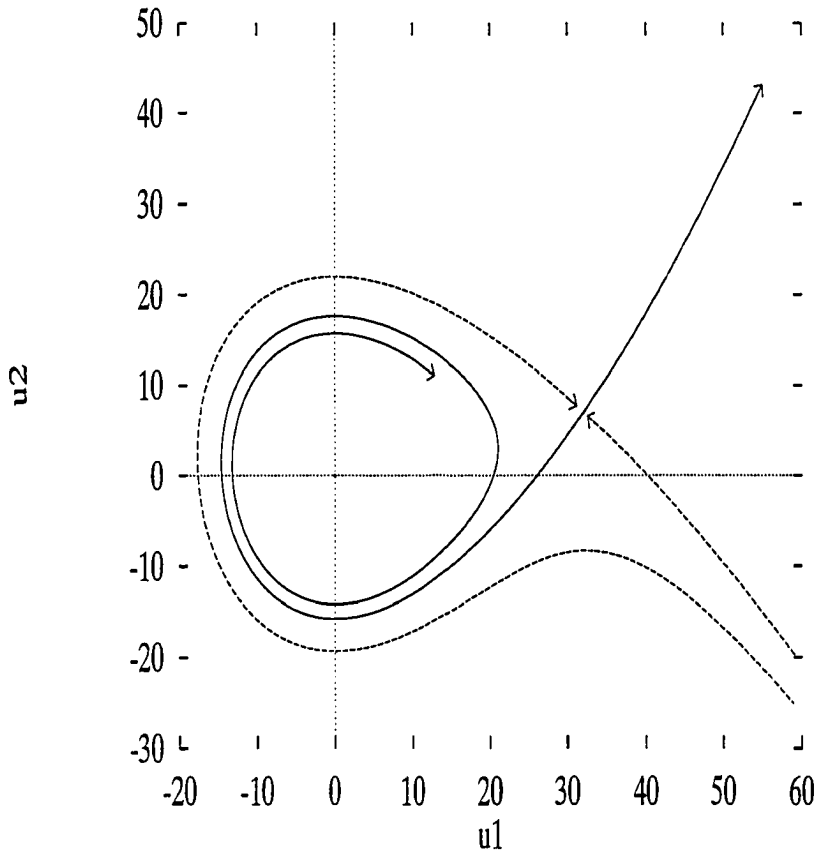


Figure 2.6: Phase trajectory in  $u(\text{yr}^2/\text{K})$  coordinates showing the topology for  $\omega = 2\pi/5700(\text{yr}^{-1})$ .

where  $\|\mathbf{u}\|_{\mathbf{u}} = \sqrt{u_1^2 + u_2^2}$  is the Euclidean norm in  $\mathbf{u}$  coordinates. When this is done, we get the approximation

$$\omega_{min}^2 = \frac{8F^3 T_e^5 \kappa^2 (2RT_e + 8LR\kappa T_e^4 + 3F)}{1 + 4\kappa T_e^3 L} a + O(a^2) + O(\omega^4). \quad (2.4.7)$$

In Fig. 2.7 we set  $a = 0.1(\text{yr}^2/^\circ\text{K})$  and plot  $P_{max} = 2\pi/\omega_{min}$  as a function of equilibrium temperature  $T_e$ . Notice that this period is governed in magnitude by a factor of  $1/\sqrt{a}$ .

Let us now examine how the saddle manifolds behave as  $\omega$  approaches  $\omega_{min}$ . For  $T_e = 246(^\circ\text{K})$ , we have  $\omega_{min} = 2\pi/102,681(\text{yr}^{-1})$ . We will see that this value is too small.

The stable and unstable manifolds of the second equilibrium are shown in Fig. 2.8 for  $\omega = 2\pi/20,000(\text{yr}^{-1})$ . In Fig. 2.9 we decrease  $\omega$  to  $2\pi/50,000(\text{yr}^{-1})$  and see the periodic orbit approach the saddle manifolds. When  $\omega = 2\pi/120,000(\text{yr}^{-1})$  the inflowing and outflowing manifolds cross each other, as seen in Fig. 2.10. Since the manifolds depend continuously upon  $\omega$ , we conclude they must intersect for some value between  $2\pi/50,000(\text{yr}^{-1})$  and  $2\pi/120,000(\text{yr}^{-1})$  to form a homoclinic orbit.

Finding the exact value of  $\omega$  via computer experiments is not, in general, possible. We may get very close by observing the crossing of the inflowing and outflowing manifolds and adjusting  $\omega$  appropriately, essentially a bisection technique. It should be clear that even if such a value of  $\omega$  were determined to arbitrary precision, computer roundoff will not allow a simulation of a true homoclinic orbit. For

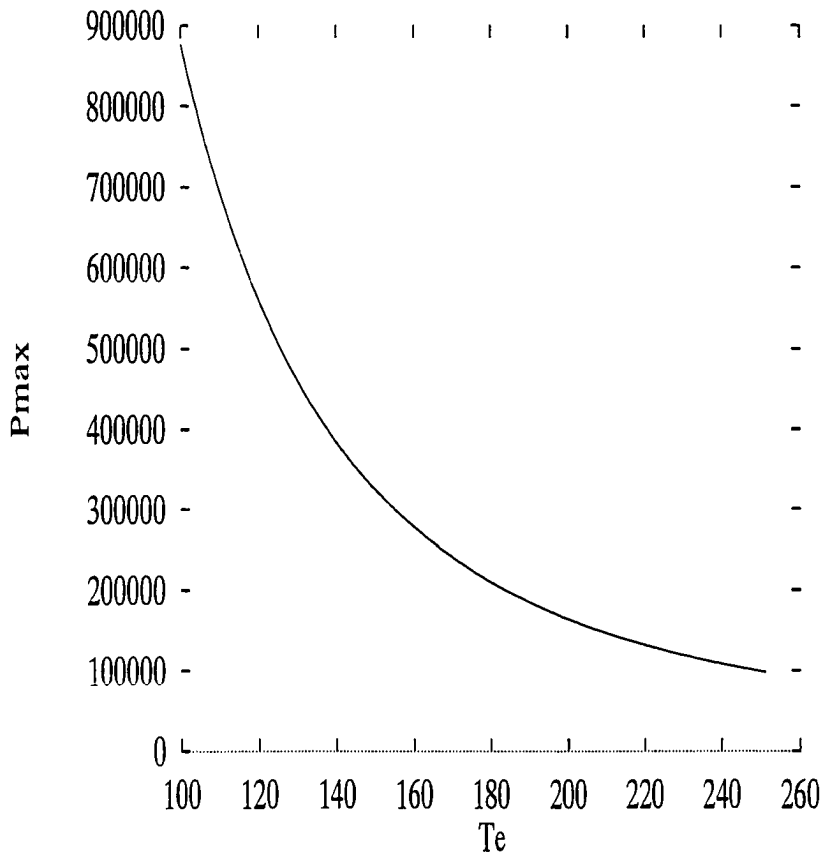


Figure 2.7: Maximum period  $P_{max}$  (yr) plotted verses equilibrium temperature  $T_e$  (°K) with  $a = 0.1$  (yr<sup>2</sup>/°K).

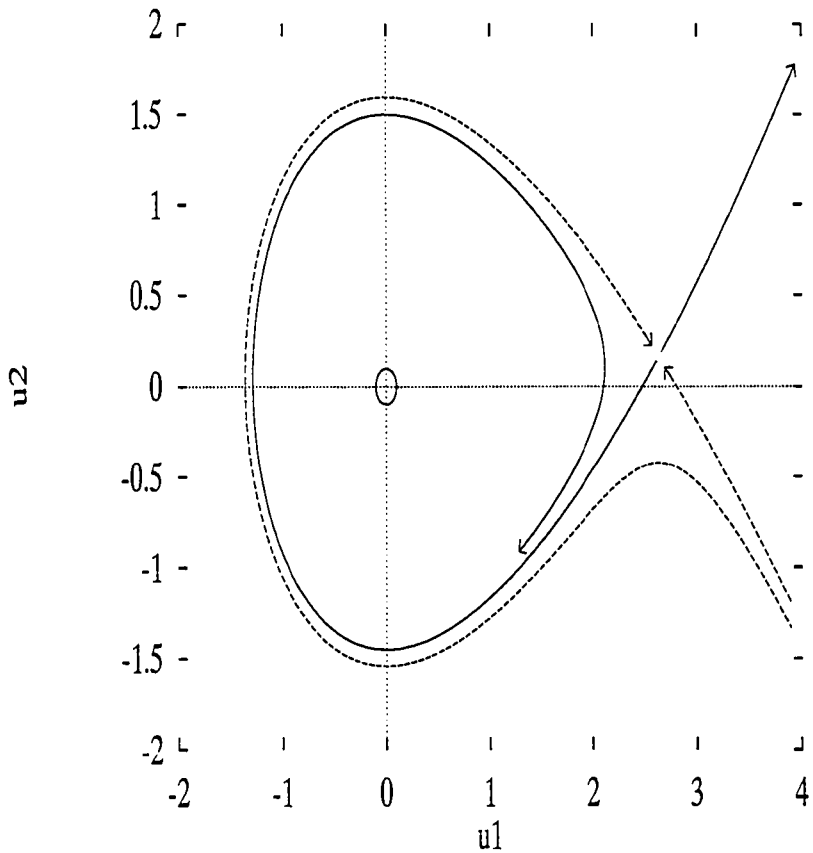


Figure 2.8: Inflowing and outflowing manifolds of the second equilibrium and the periodic orbit about the chosen equilibrium in  $\mathbf{u}(\dot{\text{yr}}^2/\text{°K})$  coordinates for  $\omega = 2\pi/20,000(\text{yr}^{-1})$ . The attracting region for the periodic orbit is bounded by the two inflowing manifolds.

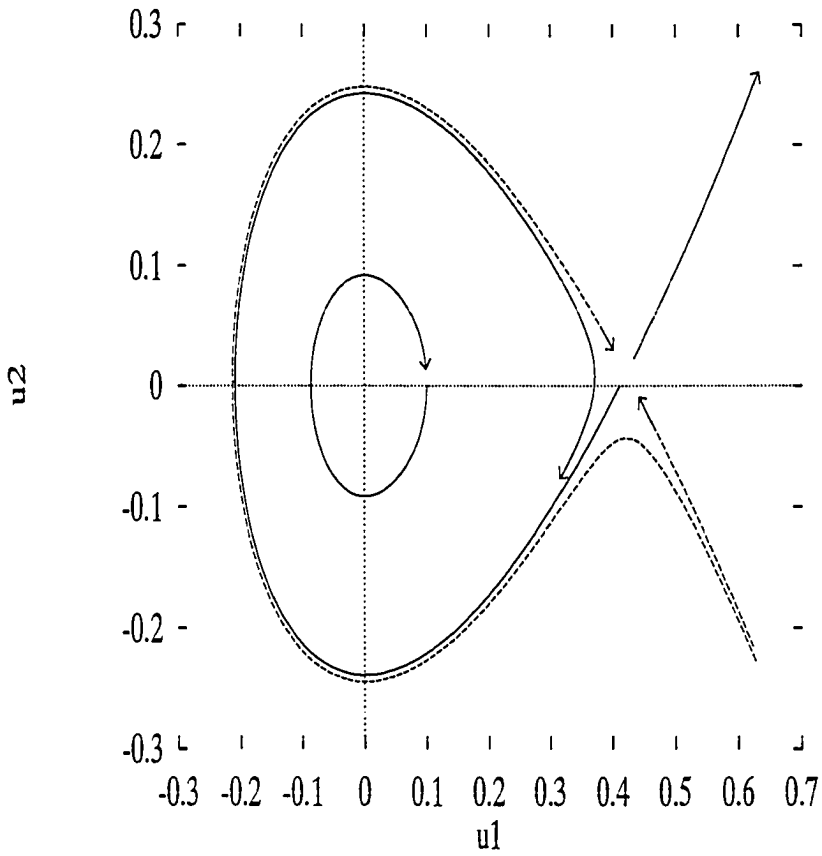


Figure 2.9: Inflowing and outflowing manifolds of the second equilibrium and the periodic orbit about the chosen equilibrium in  $u$  ( $\text{yr}^2/\text{K}$ ) coordinates for  $\omega = 2\pi/50,000(\text{yr}^{-1})$ .

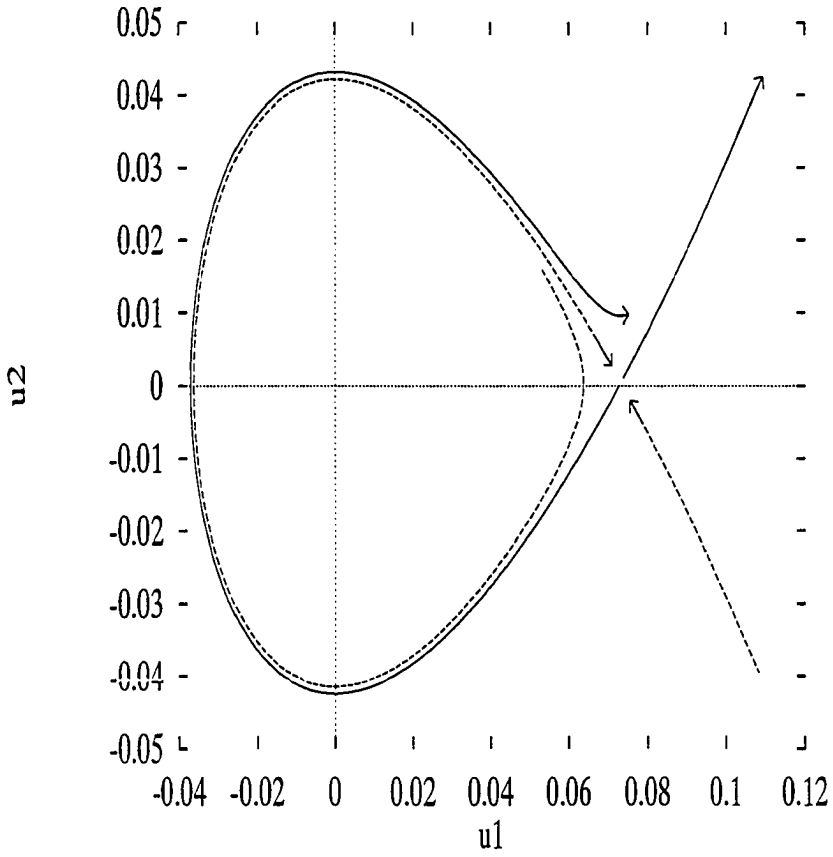


Figure 2.10: Crossing of the inflowing and outflowing manifolds of the second equilibrium in  $u$  ( $\text{yr}^2/\text{K}$ ) coordinates for  $\omega = 2\pi/120,000(\text{yr}^{-1})$ .

the parameters selected, the inflowing and outflowing manifolds intersect between  $\omega = 2\pi/89,276(\text{yr}^{-1})$  and  $\omega = 2\pi/89,277(\text{yr}^{-1})$ . Fig. 2.11 shows the approximate homoclinic orbit.

When  $\omega = 2\pi/89,276(\text{yr}^{-1})$ , the local phase space topology is that of Fig. 2.8 and Fig. 2.9 where the periodic orbit attracts in positive time and the attracting region for this periodic orbit is bounded between the two inflowing manifolds.

When  $\omega = 2\pi/89,277(\text{yr}^{-1})$ , the local phase space topology is that of Fig. 2.10 where the periodic orbit attracts in negative time and solutions leave this orbit in positive time through the region bounded by the two outflowing manifolds. Details of the types of structures that bifurcate from the intersection of inflowing and outflowing manifolds can be found in [2].

A short time series for all four of the saddle manifolds are shown with  $\omega = 2\pi/89277(\text{yr}^{-1})$  in Fig. 2.12 and with  $\omega = 2\pi/89276(\text{yr}^{-1})$  in Fig. 2.13.

## 2.5 Linear verses nonlinear periods

The parameter  $\omega$  gives the rotation rate of solutions to the linearized equations about the chosen constant equilibrium. This  $\omega$  value also corresponds asymptotically to the rotation rate of solutions to the nonlinear equations initially near the equilibrium. However the frequency of the periodic orbit we obtained for the nonlinear equations differs from the value of  $\omega$ , especially as  $\omega \rightarrow \omega_{min}$ . This is expected, since the period of the homoclinic orbit is infinite. Because the period of the orbit varies smoothly

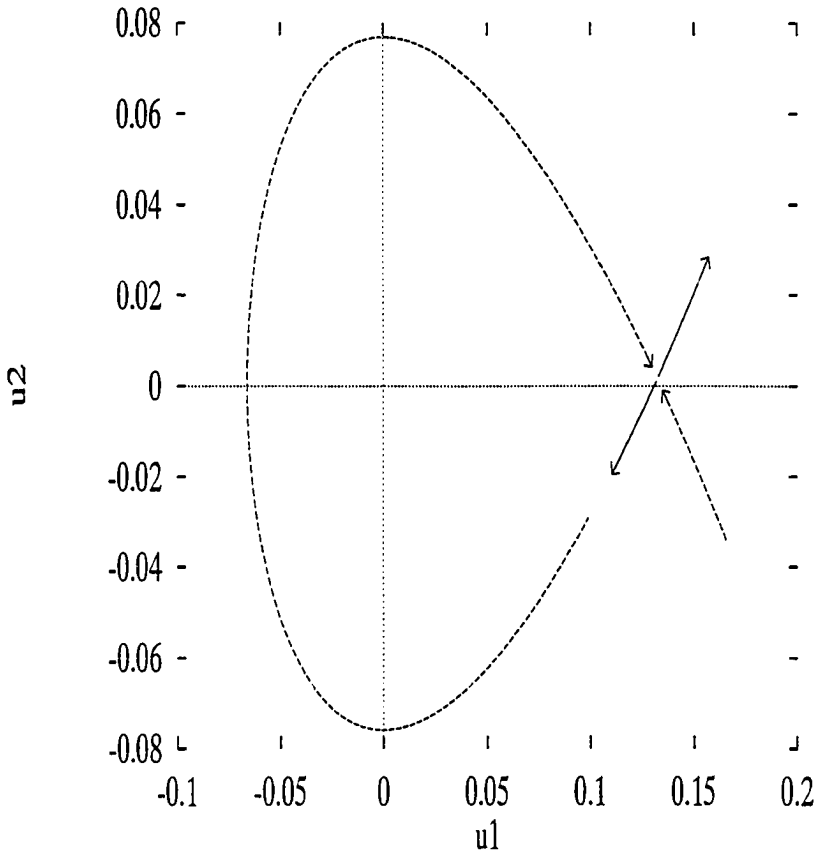


Figure 2.11: Inflowing and outflowing manifolds in  $u$  ( $\text{yr}^2/\text{°K}$ ) coordinates at the approximate intersection value of  $\omega = 2\pi/89277(\text{yr}^{-1})$ .

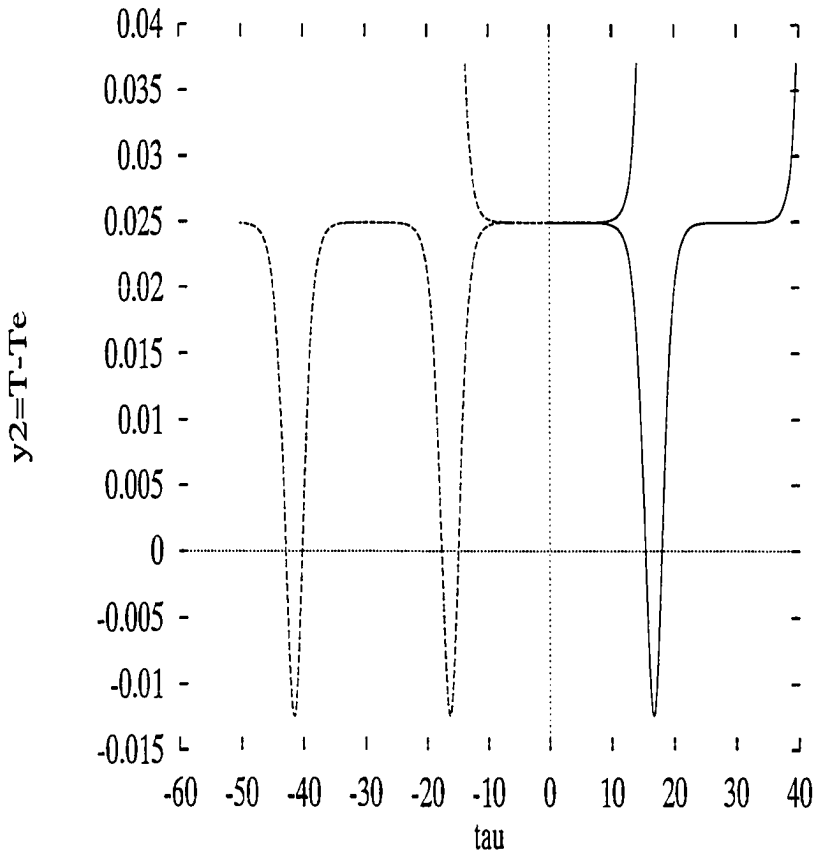


Figure 2.12: The time series  $y_2$  ( $^{\circ}\mathbf{K}$ ) vs  $\tau$  (*unitless*) of the saddle manifolds for  $\omega = 2\pi/89277(\text{yr}^{-1})$ . The periodic orbit bifurcating from the homoclinic orbit attracts in negative time.

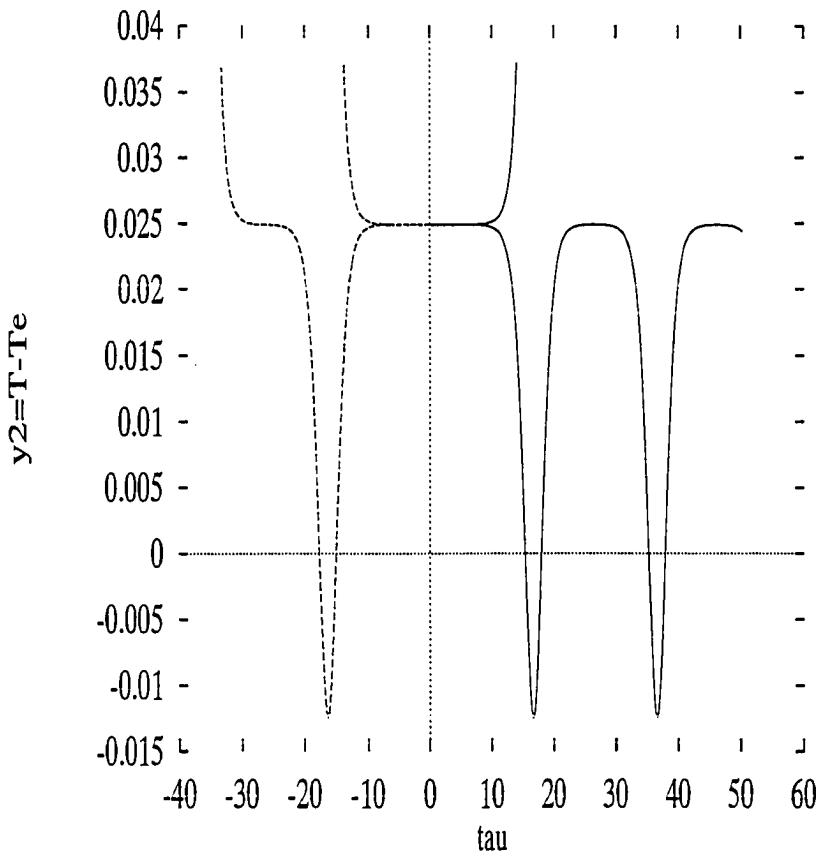


Figure 2.13: The time series  $y_2$  ( $^{\circ}\mathbf{K}$ ) vs  $\tau$  (*unitless*) of the saddle manifolds for  $\omega = 2\pi/89276(\text{yr}^{-1})$ . The periodic orbit bifurcating from the homoclinic orbit attracts in positive time.

with the parameters, we can plot the nonlinear period as a function of  $\omega$ .

By calculating the fixed point of the Poincaré map, we can determine the period of the nonlinear periodic orbit. We use the line  $u_1 = 0$  for calculating the Poincaré map. Geometrically, the Poincaré map of any point  $\mathbf{u}(0)$  lying on the line  $u_1 = 0$ , is given by  $\mathbf{u}(t_{Poinc}) \equiv \Pi \mathbf{u}(0)$ , where  $t_{Poinc}$  is the smallest time needed for the solution to cross the line  $u_1 = 0$  again. This process is depicted in the sketch Fig. 2.14.

The initial condition of the fixed point in  $\mathbf{y}$  coordinates is given by

$$\mathbf{y}(0) = a_{fixed} \mathbf{P}^{-1} \begin{bmatrix} 1 \\ 0 \end{bmatrix}. \quad (2.5.8)$$

where  $a_{fixed}$  is such that  $\mathbf{y}(t_{period}) = \mathbf{y}(0)$  and  $t_{period}$  gives the first intersection of  $\mathbf{y}(t)$  with  $\mathbf{y}(0)$ . For larger  $\omega$  values,  $t_{period} \simeq 2\pi/\omega$ . However, as Fig. 2.15 shows, there is considerable difference between  $2\pi/\omega$  and  $t_{period}$ .

## 2.6 Wave forms as a function of $\omega$

We now consider the magnitude and shape of the wave representing the deviations from equilibrium for the temperature,  $y_2$ , and the glaciation,  $y_1$ , as  $\omega$  decreases from the maximum to the minimum value.

We have determined the approximate  $\lambda(a)$  giving a periodic orbit of radius  $a$  in  $\mathbf{u}$  coordinates by (C.11). However, to relate this to physically meaningful coordinates, we need to determine how this orbit maps to  $\mathbf{y}$  coordinates. Using  $\mathbf{y} = \mathbf{P}\mathbf{u}$  and  $r = a$

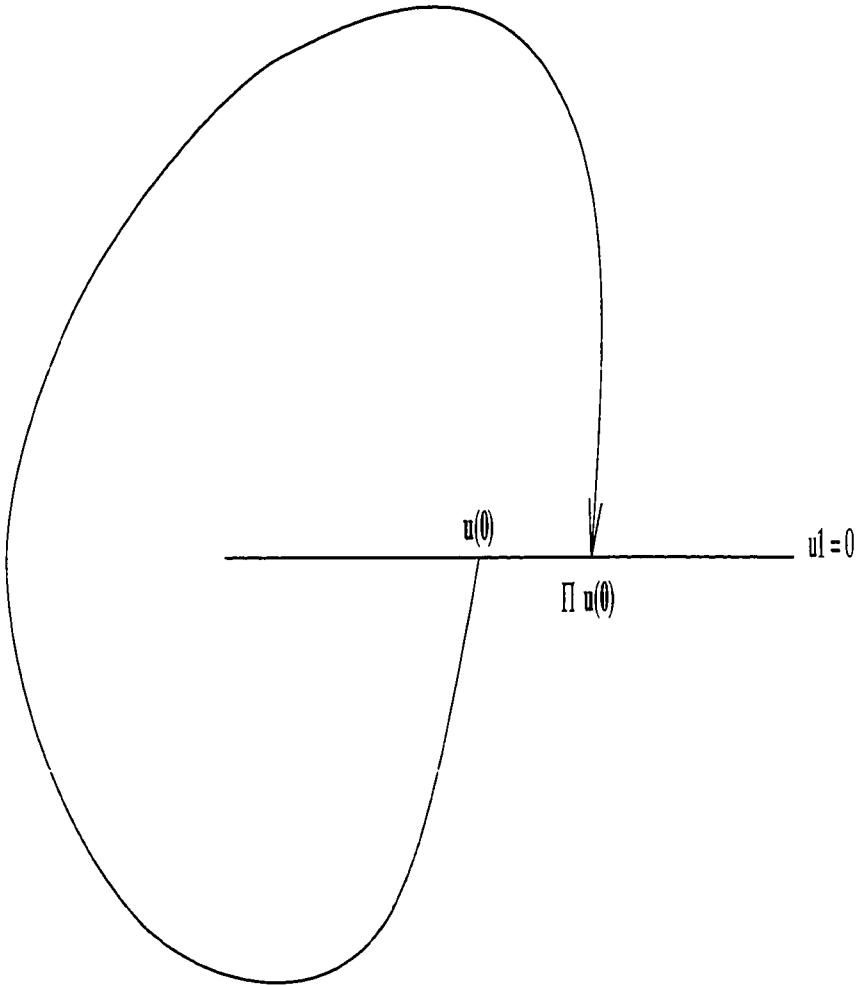


Figure 2.14: Geometric sketch of the Poincaré map for a two dimensional phase trajectory.

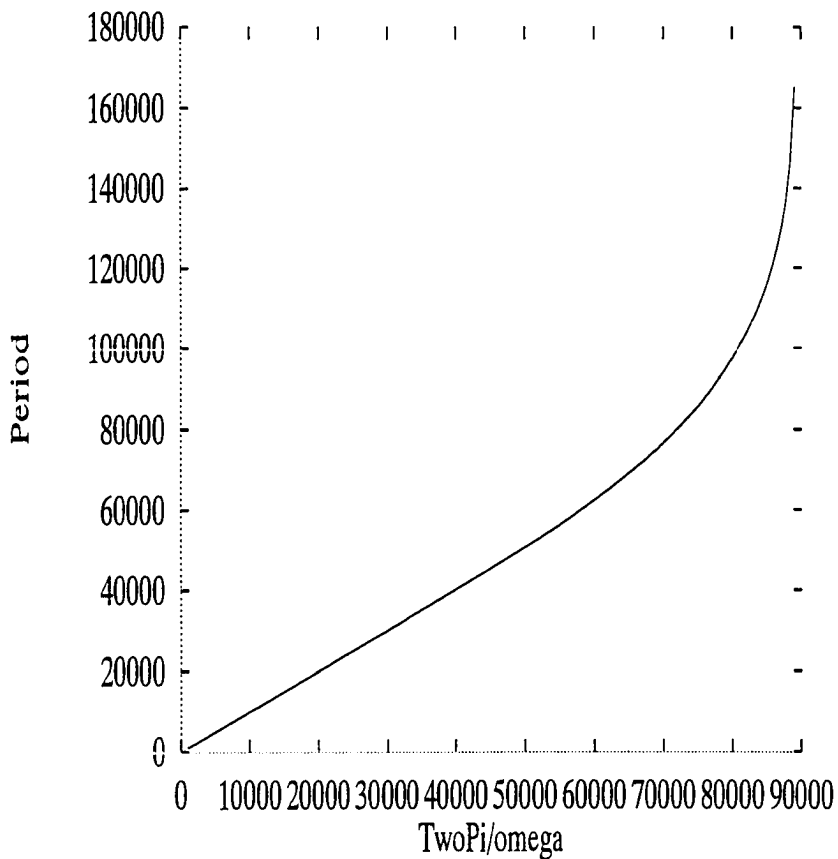


Figure 2.15: Period (yr) of the periodic orbit plotted verses  $2\pi/\omega(\text{yr})$ . Solutions near the equilibrium (inside the periodic orbit) will rotate at the rate of  $2\pi/\omega(\text{yr})$  initially. However, at  $t \rightarrow \infty$ , the rotation rate slows to the given period value as it approaches the periodic orbit.

in (C.3) we see that

$$\begin{aligned}
 y_{periodic} = & \begin{bmatrix} -4 \kappa F^2 T_e^3 + L\omega^2 \\ L^2\omega^2 + F^2 \end{bmatrix} a \cos(\theta) \\
 + & \begin{bmatrix} F\omega + 4 F\omega \kappa T_e^3 L \\ 0 \end{bmatrix} a \sin(\theta) + \begin{bmatrix} O(a^3) \\ O(a^3) \end{bmatrix}
 \end{aligned} \tag{2.6.9}$$

where  $\theta = \theta(t)$ . The approximate maximum deviation from equilibrium temperature is then

$$T_{max} = (L^2\omega^2 + F^2) a \tag{2.6.10}$$

and the approximate maximum deviation from glaciation equilibrium is

$$G_{max} = T_{max} \sqrt{\frac{16 \kappa^2 F^2 T_e^6 + \omega^2}{L^2\omega^2 + F^2}}. \tag{2.6.11}$$

In Fig. 2.16 and Fig. 2.17 we set  $a = 0.1 \text{ (yr}^2/\text{°K)}$  and  $T_e = 246 \text{ (°K)}$  (equilibrium glaciation  $G_e = 1 - \kappa T_e^4 = 0.0970$ ) to plot these deviations from  $P_{min}$  to  $P_{max}$ .

There is good agreement in the shape of the periodic wave corresponding to the fixed point of the Poincare map and the approximation in (2.6.9) for  $\omega$  values in Fig. 2.15 where the period  $\simeq 2\pi/\omega$ . With the parameters chosen, this period is less than about 70,000(yr). This is, of course, due to the fact that the second equilibrium is rather distant from the periodic orbit and the linear approximation agrees with the nonlinear dynamics.

However, as the proximity of the second equilibrium approaches the periodic orbit, the resultant wave form deviates from the linear approximation. In Fig. 2.18 and

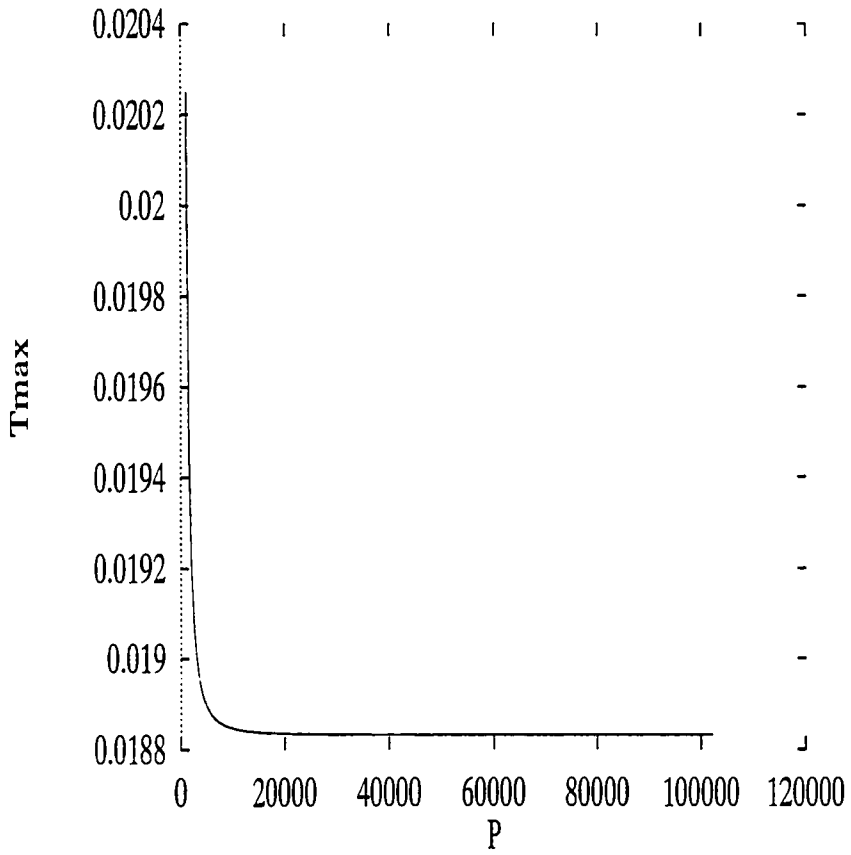


Figure 2.16: Maximum temperature deviation from equilibrium  $T_{max}$  (°K) plotted from  $P_{min}$  (yr) to  $P_{max}$  (yr) with  $T_e = 246$  (°K) and  $a = 0.1$  (yr<sup>2</sup>/°K).

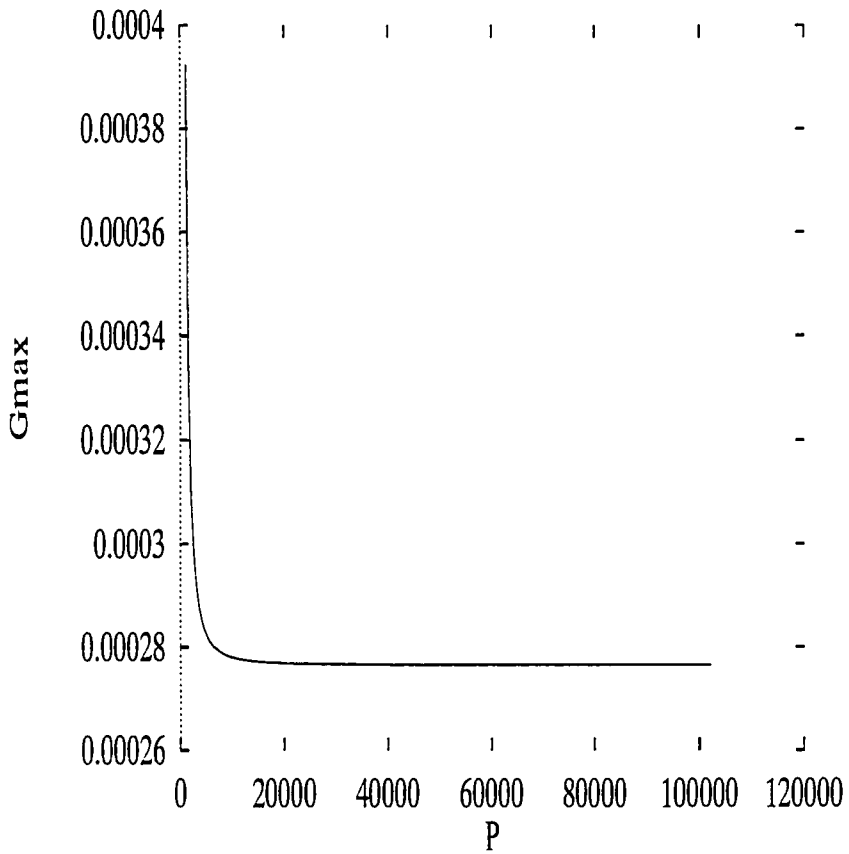


Figure 2.17: Maximum glaciation deviation from equilibrium  $G_{max}$  plotted from  $P_{min}$  (yr) to  $P_{max}$  (yr) with  $T_e = 246$  ( $^{\circ}\mathbf{K}$ ) and  $a = 0.1$  ( $\text{yr}^2/^{\circ}\mathbf{K}$ ).

Fig. 2.19 we show the wave forms as a function of  $\theta = 2\pi t/t_{period}$  where  $t_{period}$  is defined in (2.5.8). In both figures,  $\theta$  goes from 0 to  $4\pi$  thereby showing two wave forms. The three  $\omega$  values shown are  $\omega_1 = 2\pi/70,000(\text{yr}^{-1})$ ,  $\omega_2 = 2\pi/79,600(\text{yr}^{-1})$ , and  $\omega_3 = 2\pi/89,200(\text{yr}^{-1})$ ; the rotation rate of the linearized equations increase uniformly by  $9,600(\text{yr})$ . However, as Fig. 2.15 shows, the period of the nonlinear equations increases much more than the rotation rate of the linearized equations. From  $\omega_1$  to  $\omega_2$  the period increases by approximately  $20,000(\text{yr})$ ; from  $\omega_2$  to  $\omega_3$  the period increases by approximately  $70,000(\text{yr})$ .

The phase portrait in  $y$  coordinates for the minimum and maximum  $\omega$  are shown in Fig 2.20. Notice the distortion in the ellipse when the second equilibrium is near the periodic orbit at the minimum  $\omega$  value.

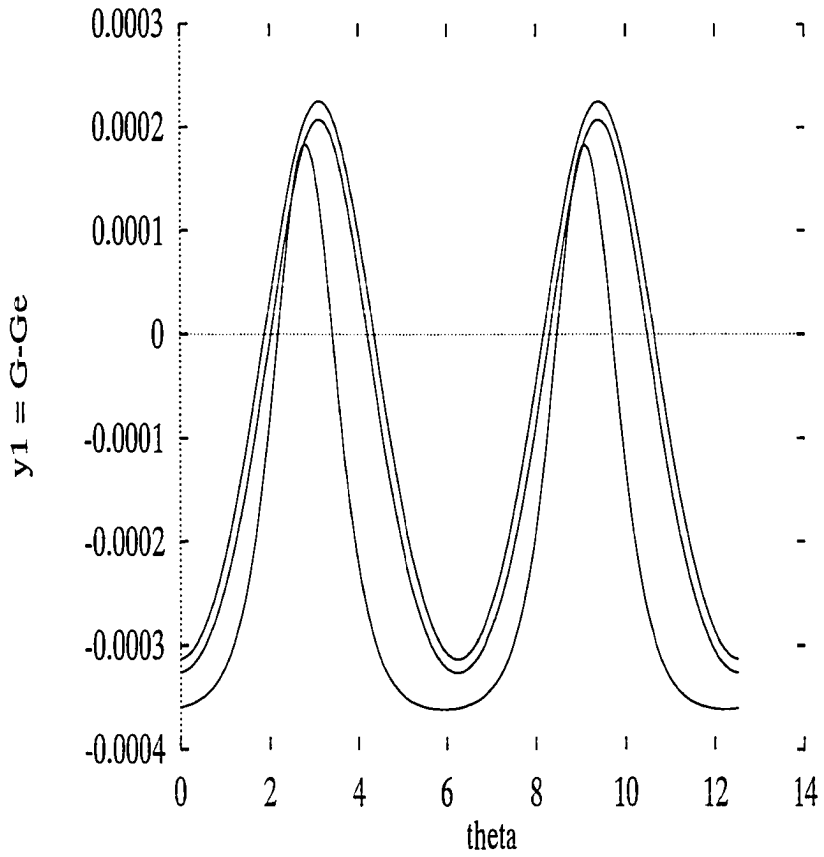


Figure 2.18: Wave forms in glaciation for  $\omega_1 = 2\pi/70,000(\text{yr}^{-1})$  (top wave),  $\omega_2 = 2\pi/79,600(\text{yr}^{-1})$  (middle wave), and  $\omega_3 = 2\pi/89,200(\text{yr}^{-1})$  (bottom wave) with  $T_e = 246(^{\circ}\text{K})$  and  $u = 0.1(\text{yr}^2/^{\circ}\text{K})$ .

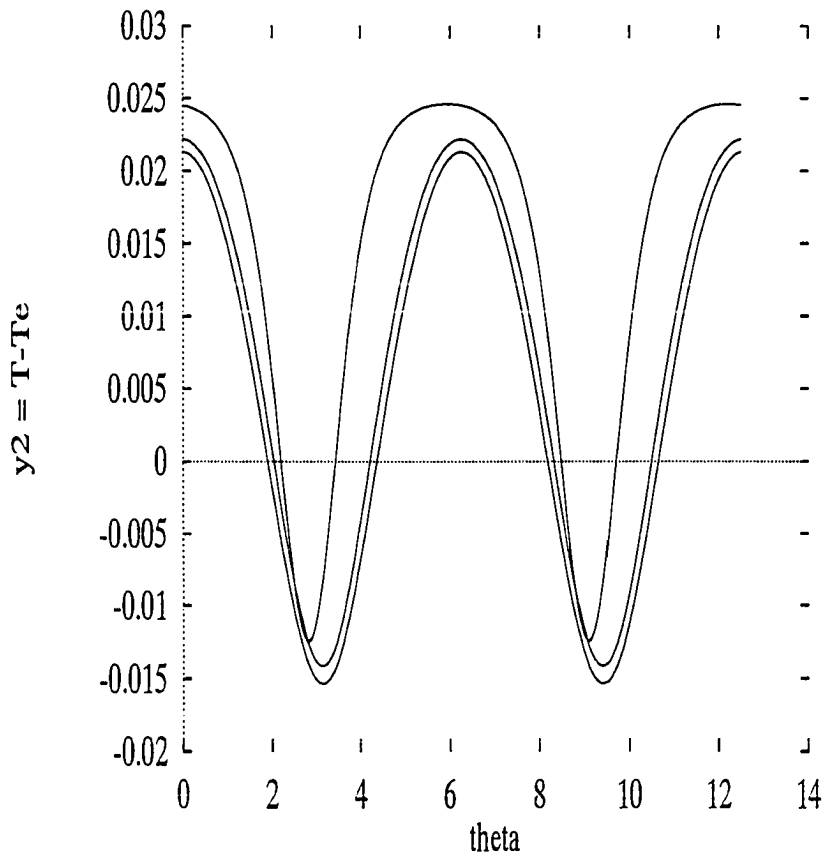


Figure 2.19: Wave forms in temperature for  $\omega_1 = 2\pi/70,000(\text{yr}^{-1})$  (bottom wave),  $\omega_2 = 2\pi/79,600(\text{yr}^{-1})$  (middle wave), and  $\omega_3 = 2\pi/89,200(\text{yr}^{-1})$  (top wave) with  $\bar{T}_e = 246(^{\circ}\bar{\mathbf{K}})$  and  $a = 0.1(\text{yr}^2/^{\circ}\bar{\mathbf{K}})$ .

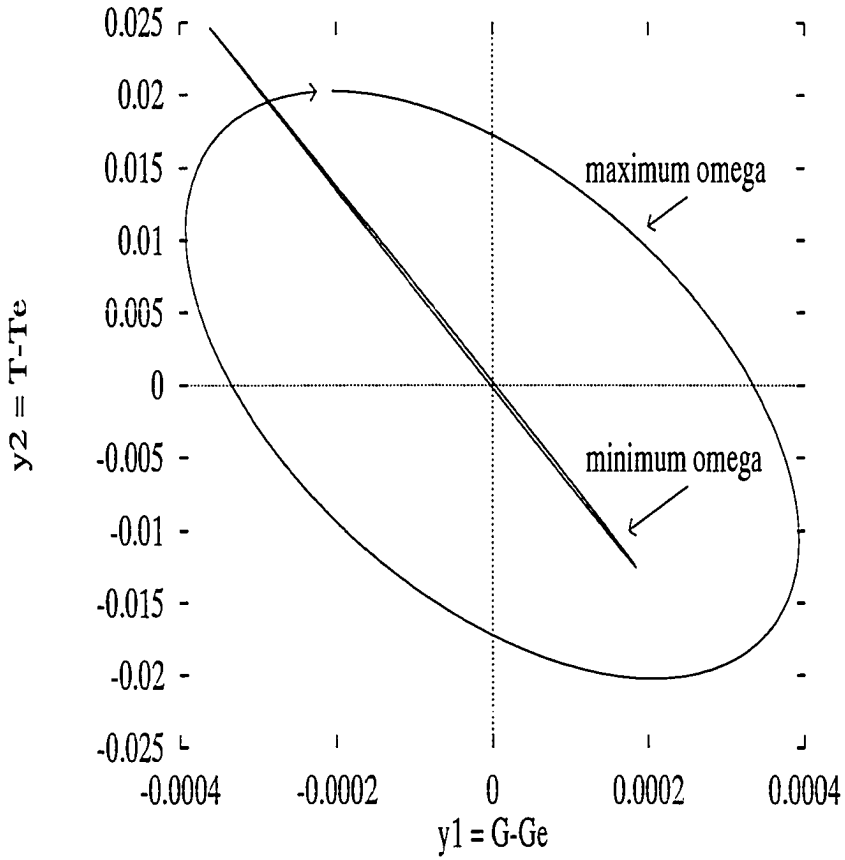


Figure 2.20: Phase trajectory in  $\mathbf{y}$  for the maximum and minimum  $\omega$  values  $\omega_{max} = 2\pi/1055(\text{yr}^{-1})$  and  $\omega_{min} \simeq 2\pi/89,200(\text{yr}^{-1})$  with  $T_e = 246(^{\circ}\mathbf{K})$  and  $a = 0.1(\text{yr}^2/^{\circ}\mathbf{K})$ .

# Chapter 3

## Periodic Orbital Variation

### 3.1 Introduction

We consider how orbital variation affects the stable constant equilibrium by allowing periodic modulation of the parameter  $B$  as described in Sect. 1.2. The deviation equations are given by (1.2.7). The phase space of the differential equations is now  $\mathcal{R}^2 \times \mathcal{S}^1$  and the dynamics can be studied using the Poincaré map defined by

$$\Pi \mathbf{y}(0) = \mathbf{y}(2\pi/\sigma) \quad (3.1.1)$$

where  $\mathbf{y}(t)$  is the solution to (1.2.7).

The linearized equations

$$\dot{\mathbf{y}} = \hat{\mathbf{A}}(\sigma t, \delta) \mathbf{y} \quad (3.1.2)$$

where  $\hat{\mathbf{A}}(\sigma t, \delta)$  is given by (1.2.8) allow us to determine the character of the linearized Poincaré map using Floquet theory.

Once this character is determined, the invariant manifolds of the nonlinear equations may be studied by using information provided by the linearized approximation. Determining the Floquet monodromy matrix analytically is in general not feasible. We will calculate this matrix numerically.

To obtain behavior different from the self sustained oscillations, we seek parameter modulations such that the eigenvalues of the monodromy matrix are both real. Of course if both eigenvalues have magnitude less than 1, then the invariant set is still the equilibrium  $\mathbf{y} = 0$ .

As an eigenvalue passes through 1 or -1, while the other eigenvalue is not of unit magnitude, a saddle node bifurcation of the nonlinear Poincaré map typically occurs. For an eigenvalue passing through 1, the fixed point of the Poincaré map along the outflowing manifold produces structurally stable periodic motion at the frequency of modulation. For eigenvalues passing through -1, the typical bifurcation is that of structurally stable periodic motion at twice the modulation frequency; the fixed point occurs for two iterations of the map. The eigenvectors of the monodromy matrix provides us with initial conditions to study the nonlinear Poincaré map.

## 3.2 The eigenvalues of the monodromy matrix

We consider the dynamics of the linear system (3.1.2). What type of bifurcation can we expect? If  $\sigma = 0$ , then the resulting autonomous system bifurcates to a saddle for

$\delta > \delta_{autobif}$  where

$$\delta_{autobif} = \frac{\omega^2 + \alpha^2}{F} \quad (3.2.3)$$

Of course nonautonomous equations, regardless of how small  $\sigma$  is, do not bifurcate as the autonomous equations. If the matrix  $\hat{\mathbf{A}}(\sigma t, \delta)$  in (1.2.8) was symmetric in the time dependence, then we could study  $\delta_{bif}(\sigma)$  analytically. However this is not the case, and it serves our purposes to treat  $\sigma$  as fixed and consider  $\delta$  a bifurcation parameter for the eigenvalues of the monodromy matrix. These eigenvalues must be calculated numerically.

Since the external frequency  $\sigma = 2\pi/20,000(\text{yr}^{-1})$  is fixed, we will consider the internal frequency  $\omega$  also as a bifurcation parameter. Let  $\mathbf{M}(\omega, \delta)$  be the monodromy matrix of the linear system (3.1.2) corresponding to the 20,000 year periodic coefficients. Necessary details of Floquet theory are given in Appendix E. The linearized Poincaré map is then given by

$$\Pi_{lin} \mathbf{y}(0) = \mathbf{M} \mathbf{y}(0) \quad (3.2.4)$$

The eigenvalues of the matrix  $\mathbf{M}(\omega, \delta)$  will determine the stability of (3.2.4) and hence the stability of (3.1.2). Let  $\gamma_{1,2}(\omega, \delta)$  denote these eigenvalues.

We know exactly  $\gamma_{1,2}(\omega, 0)$ . Specifically the matrix  $\mathbf{M}(\omega, 0)$  is  $e^{\mathbf{A}2\pi/\sigma}$ . The eigenvalues of this matrix are the same as the eigenvalues of the matrix  $e^{\mathbf{J}2\pi/\sigma}$  where

$$\mathbf{J} = \begin{bmatrix} \alpha & \omega \\ -\omega & \alpha \end{bmatrix}. \quad (3.2.5)$$

Thus we have

$$\gamma_{1,2}(\omega, 0) = e^{2\pi\frac{\alpha}{\sigma}} \left( \cos\left(2\pi\frac{\omega}{\sigma}\right) \pm i \sin\left(2\pi\frac{\omega}{\sigma}\right) \right) \quad (3.2.6)$$

This will allow us to analytically locate the initial point on the bifurcation curve. The relationship between the internal frequency  $\omega$  and the external modulation frequency  $\sigma$  can be seen by examining (3.2.6). Clearly, the magnitude of  $\gamma_{1,2}(\omega, 0)$  are less than 1 since  $\alpha < 0$ . However the sign of  $Re(\gamma_{1,2}(\omega, 0))$  depends upon the sign of  $\cos(2\pi\omega/\sigma)$ .

What is the significance of the sign of the eigenvalues at the time of bifurcation to a saddle? With a saddle type equilibrium, the linear system is unstable if  $|\gamma_{1,2}(\omega, \delta)| > 1$  regardless of the sign of these quantities. However, the sign does play an important role in determining characteristics of the nonlinear map which can bound these instabilities.

Assuming the slope of the bifurcation curve for  $Re(\gamma_{1,2}(\omega, 0))$  remains relatively constant until bifurcation to a saddle, we can identify likely values of  $\omega$  that produce the negative eigenvalues identified with period doubling.

If  $\cos(2\pi\omega/\sigma) = 0$ , then  $\omega = \frac{1}{4}\sigma, \frac{3}{4}\sigma, \frac{5}{4}\sigma, \frac{7}{4}\sigma, \dots$  For  $\frac{1}{4}\sigma < \omega < \frac{3}{4}\sigma$  we have  $Re(\gamma_{1,2}(\omega, 0)) < 0$  and the modulation is superinternal. All other regions that have  $Re(\gamma_{1,2}(\omega, 0)) < 0$  correspond to subinternal modulation.

By fixing  $\sigma = 2\pi/20,000(\text{yr}^{-1})$ , the interesting range for  $\omega$  is  $2\pi/80,000(\text{yr}^{-1}) < \omega < 2\pi/26,666.\bar{6}(\text{yr}^{-1})$  for superinternal modulation and an infinite number of ranges for subinternal modulation. The first two subinternal ranges are  $2\pi/16,000(\text{yr}^{-1}) <$

$\omega < \simeq 2\pi/11429(\text{yr}^{-1})$  and  $2\pi/8,888.\bar{8}(\text{yr}^{-1}) < \omega < 2\pi/7,272.\bar{7}2(\text{yr}^{-1})$ . Although  $\omega$  values in these ranges do not ensure negative real eigenvalues upon bifurcation, they give values to investigate. Similarly, these ranges do not exclude negative real eigenvalues for  $\omega$  values outside these ranges. We set  $\lambda = -0.05$  and show bifurcation curves in Figs. 3.1 - 3.6 of  $\gamma_{1,2}(\omega, \delta)$  by fixing  $\omega$  increasing  $\delta$ .

For  $\omega = 2\pi/20,000(\text{yr}^{-1})$ , we have  $\gamma_1(\omega, 0) = \gamma_2(\omega, 0) = e^{2\pi\lambda}$ . This can be seen by examining (3.2.6) with  $\omega = \lambda/\alpha = \sigma$ . Figure 3.1 shows that they remain real until  $\gamma_1(\omega, \delta) > 1$ . Thus, the Poincaré map experiences only monotone decay until bifurcation to a saddle.

The values

$$\omega = 2\pi/21,000(\text{yr}^{-1})$$

$$\omega = 2\pi/18,000(\text{yr}^{-1})$$

$$\omega = 2\pi/16,000(\text{yr}^{-1})$$

$$\omega = 2\pi/12,500(\text{yr}^{-1})$$

$$\omega = 2\pi/26,666(\text{yr}^{-1})$$

all have  $\gamma_{1,2}(\omega, 0)$  as complex conjugate pairs. Consequently, for  $\delta$  small, the Poincaré map will experience oscillatory decay. Figures 3.2 - 3.6 show the Poincaré map will experience monotone decay upon increasing  $\delta$  until bifurcation to a saddle.

For  $\omega = 2\pi/21,000(\text{yr}^{-1})$  and  $\omega = 2\pi/18,000(\text{yr}^{-1})$ ,  $Re(\gamma_{1,2}(\omega, 0)) > 0$ ; upon bifurcation to a saddle, Figs. 3.2 - 3.3 show  $\gamma_1(\omega, \delta)$  passes through 1. Although for

$\omega = 2\pi/16,000(\text{yr}^{-1})$  we have  $\text{Re}(\gamma_{1,2}(\omega, 0)) = 0$ , Fig. 3.4 shows that  $\gamma_1(\omega, \delta)$  also passes through 1 upon bifurcation to a saddle.

We give two values of  $\omega$  that could lead to period doubling. For the value  $\omega = 2\pi/12,500(\text{yr}^{-1})$  the modulation is subinternal; for  $\omega = 2\pi/26,666(\text{yr}^{-1})$  the modulation is superinternal. Both have  $\gamma_1(\omega, \delta)$  passing through -1 upon bifurcation to a saddle as seen in Figs. 3.5 and 3.6.

Notice for the superinternal modulation in Fig 3.6 that the equilibrium becomes stable again upon increasing  $\delta$ . We will not pursue this phenomenon here, although it is interesting.

The geometry of a linear saddle map with positive eigenvalues is given by the cartoon in Fig. 3.7. The map with negative eigenvalues is shown in Fig. 3.8. To transform the Poincaré map of (3.1.2) to appropriate coordinates, we determine the matrix  $\hat{\mathbf{P}}$  such that

$$\hat{\mathbf{P}}^{-1}\mathbf{M}\hat{\mathbf{P}} = \begin{bmatrix} \gamma_1 & 0 \\ 0 & \gamma_2 \end{bmatrix} \quad (3.2.7)$$

and let

$$\mathbf{y} = \hat{\mathbf{P}}\mathbf{u}. \quad (3.2.8)$$

We will normalize the eigenvectors used to form  $\hat{\mathbf{P}}$ . Thus the coordinates  $\mathbf{u}$  will be unitless.

### 3.3 The period doubling effect

We examine the outflowing manifolds of the Poincaré map for the nonlinear system (1.2.7) with parameters such that the monodromy matrix of (3.1.2) has negative saddle eigenvalues. Saddle node bifurcation of the map corresponds to a fixed point along the outflowing manifold. For period doubling, this fixed point occurs in two iterations of the map.

The outflowing manifold is tangent at the origin to the eigenvector of the monodromy matrix corresponding to the eigenvalue with magnitude greater than 1. To find the fixed point, an initial condition is selected at a small displacement along this eigenvector. When the distance between successive double iterations is small, the period double solution is approximated.

For demonstration, we set  $\lambda = -0.05$  and select two  $(\omega, \delta)$  combinations, representing both subinternal and superinternal modulation. In both cases, the initial displacement along the eigenvector is  $10^{-6}$  and the relative tolerance for the double fixed points is  $10^{-4}$ . The outflowing manifolds are shown in the  $u$  coordinates defined by 3.2.8. Time is scaled by  $\tau = \sigma t$ .

In Fig. 3.9 the double period fixed points and the outflowing manifolds are given for  $\omega = 2\pi/12, 500(\text{yr}^{-1})$  and  $\delta/B = 0.0076$ ; the double period wave forms are given in Fig. 3.10. Figure 3.11 and Fig. 3.12 show the results for  $\omega = 2\pi/26, 666(\text{yr}^{-1})$  and  $\delta/B = 0.00272$ .

### 3.4 The geometry of chaos

We examine the geometric relationship between the inflowing and outflowing saddle manifolds of the Poincaré map for parameter values that cause these manifolds to intersect transversally. While difficult to establish, the numerical evidence indicates the existence of a transversal homoclinic point. The specific criteria for the mapping to be chaotic depends upon the images and pre-images of sector bundles, which we will not go into here. For a very thorough discussion of this topic, see [17].

Inflowing and outflowing manifolds are viewed in  $\mathbf{u}$  coordinates defined in 3.2.8. Diamonds represent integrations in positive time and pluses represent integrations done in negative time.

The parameters used are  $\lambda = -0.05$  and  $\omega = 2\pi/12,500(\text{yr}^{-1})$ . Saddle manifold structure is first shown for the nonchaotic parameter  $\delta/B = 0.0076$  corresponding to the period doubling phenomenon in Fig. 3.13. When  $\delta/B = 0.0084$ , the period doubling algorithm used in the previous section fails. Figure 3.14 indicates why. The transversal intersection of the inflowing and outflowing manifolds can be clearly seen.

To emphasize how the solutions differ for the two  $\delta/B$  values examined, we show the time series of four initial conditions for  $\delta/B = 0.0076$  in Fig. 3.15 and for  $\delta/B = 0.0084$  in Figs. 3.16 and 3.17. Two solutions are initially on one side of the outflowing manifold and two are on the other. Figure 3.15 shows solutions initially in phase along the same side of the outflowing manifold coalesce after 100 iterations of the Poincaré map. In Fig. 3.16 the solutions remain in phase after 20 iterations of the

Poincaré map. However, after 50 iterations, Fig. 3.17 shows the chaotic nature of the system.

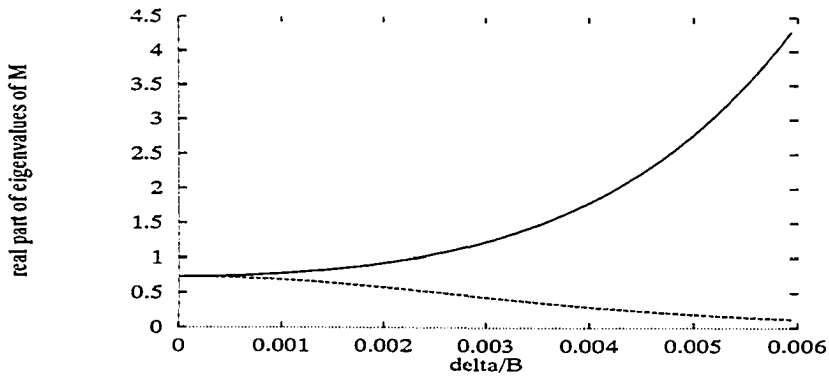


Figure 3.1: The eigenvalues  $\gamma_{1,2}(\omega, \delta)$  for  $\omega = 2\pi/20,000(\text{yr}^{-1})$  plotted against  $\delta/B$ .

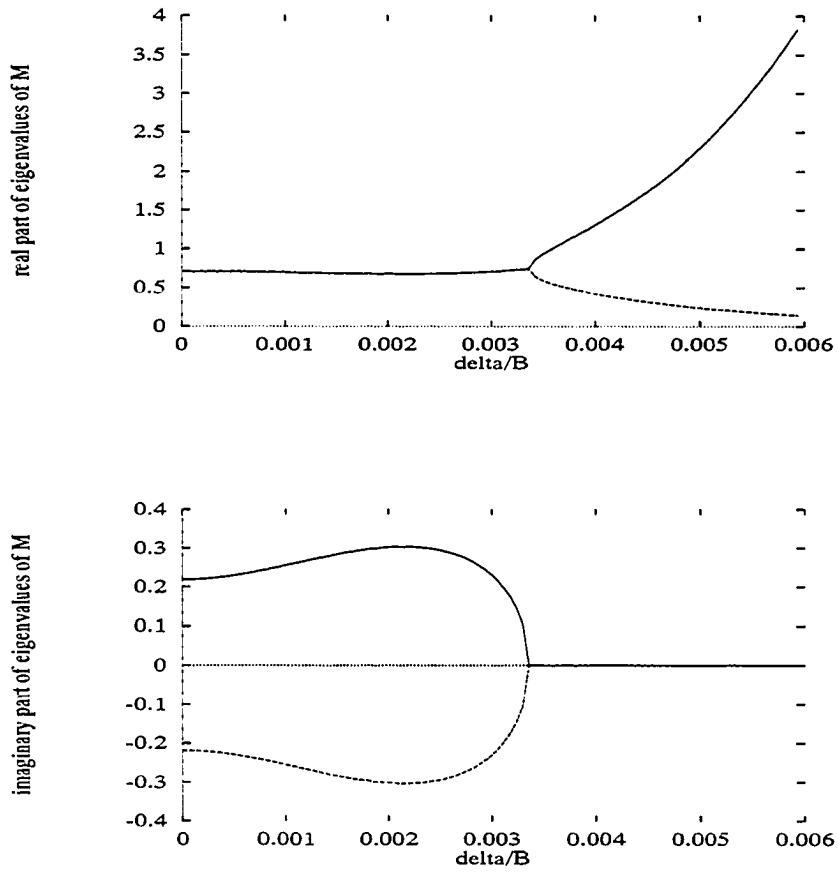


Figure 3.2: Real and imaginary parts of  $\gamma_{1,2}(\omega, \delta)$  for  $\omega = 2\pi/21,000(\text{yr}^{-1})$  plotted against  $\delta/B$ .

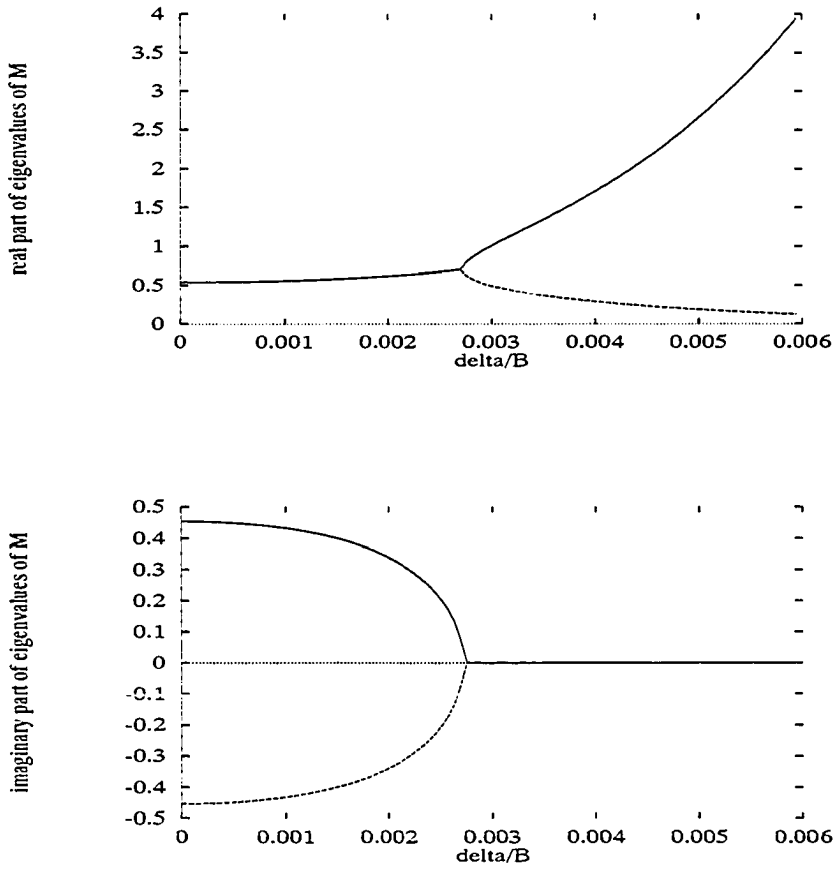


Figure 3.3: Real and imaginary parts of  $\gamma_{1,2}(\omega, \delta)$  for  $\omega = 2\pi/18,000(\text{yr}^{-1})$  plotted against  $\delta/B$ .

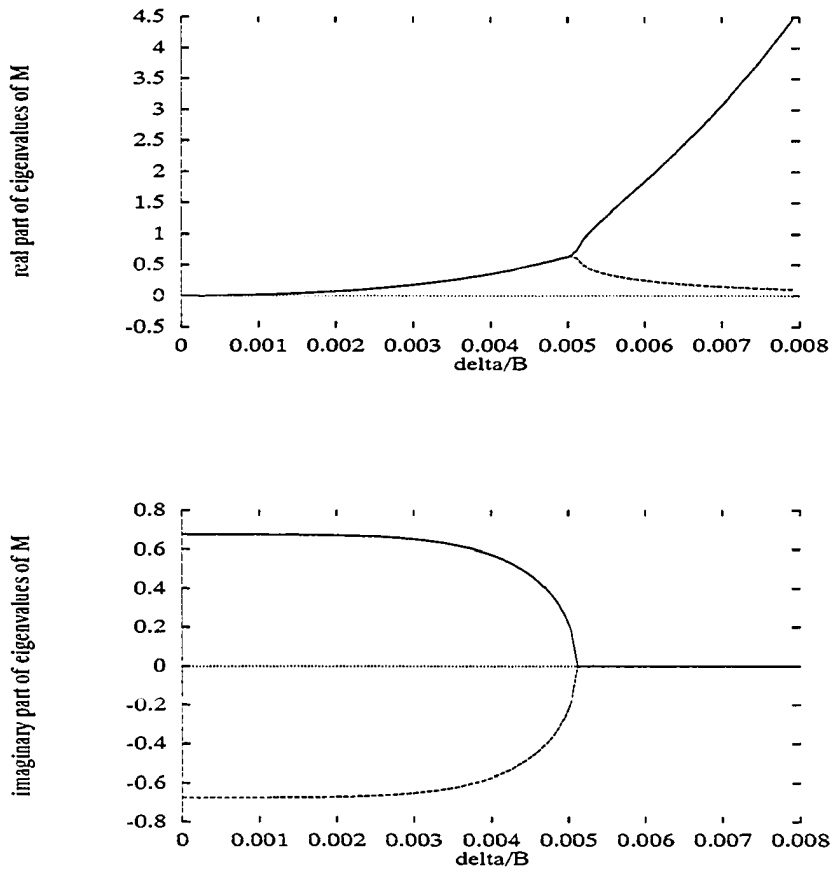


Figure 3.4: Real and imaginary parts of  $\gamma_{1,2}(\omega, \delta)$  for  $\omega = 2\pi/16,000(\text{yr}^{-1})$  plotted against  $\delta/B$ .

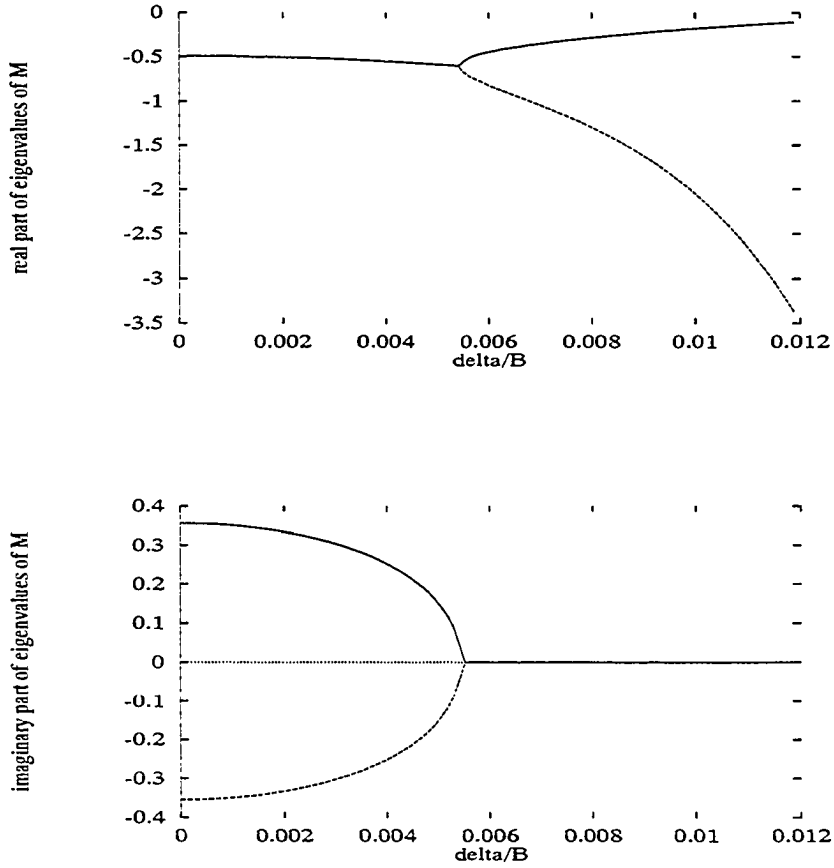


Figure 3.5: Real and imaginary parts of  $\gamma_{1,2}(\omega, \delta)$  for  $\omega = 2\pi/12,500(\text{yr}^{-1})$  plotted against  $\delta/B$ .

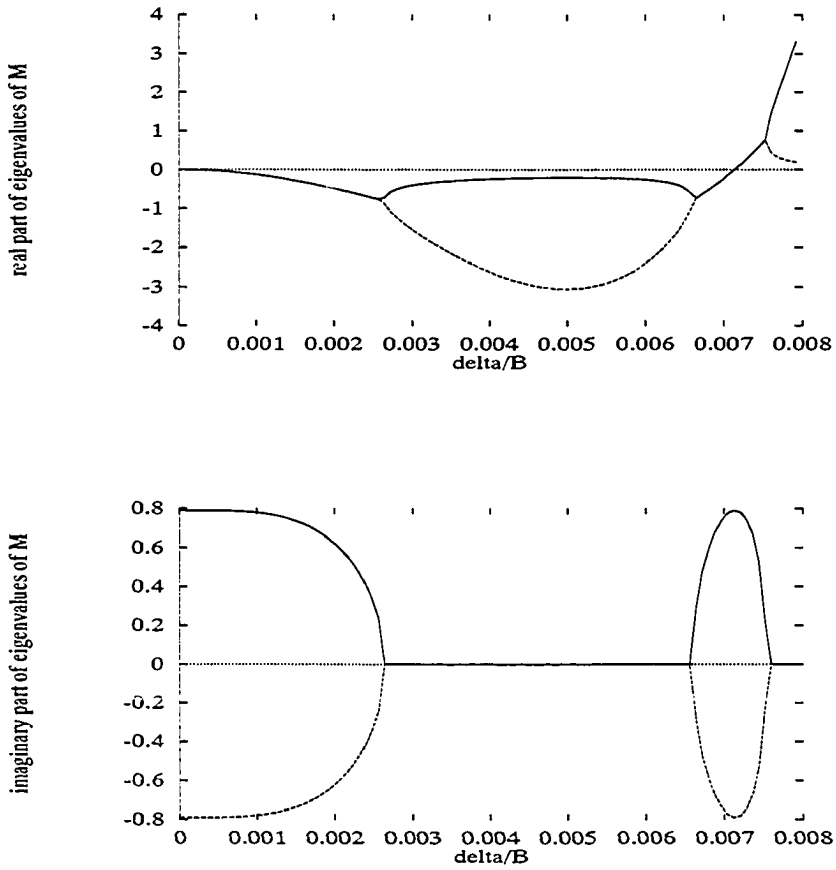


Figure 3.6: Real and imaginary parts of  $\gamma_{1,2}(\omega, \delta)$  for  $\omega = 2\pi/26,666(\text{yr}^{-1})$  plotted against  $\delta/B$ .

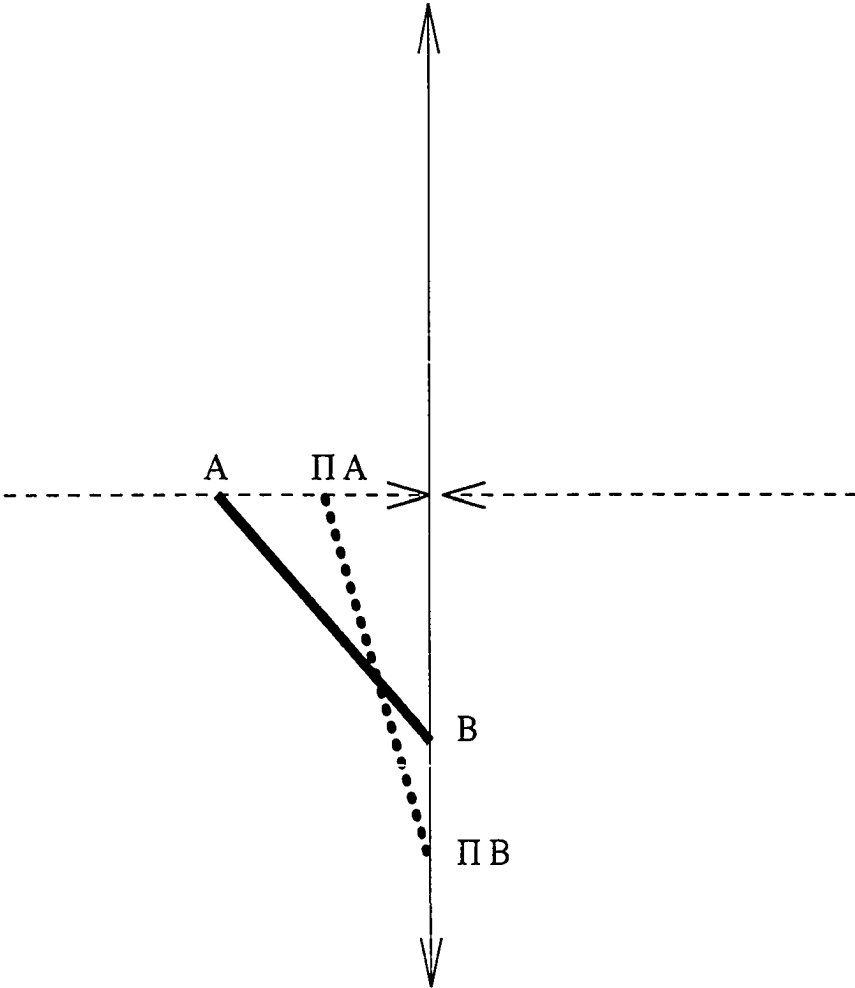


Figure 3.7: Generic mapping for a saddle type linear map with two positive eigenvalues.

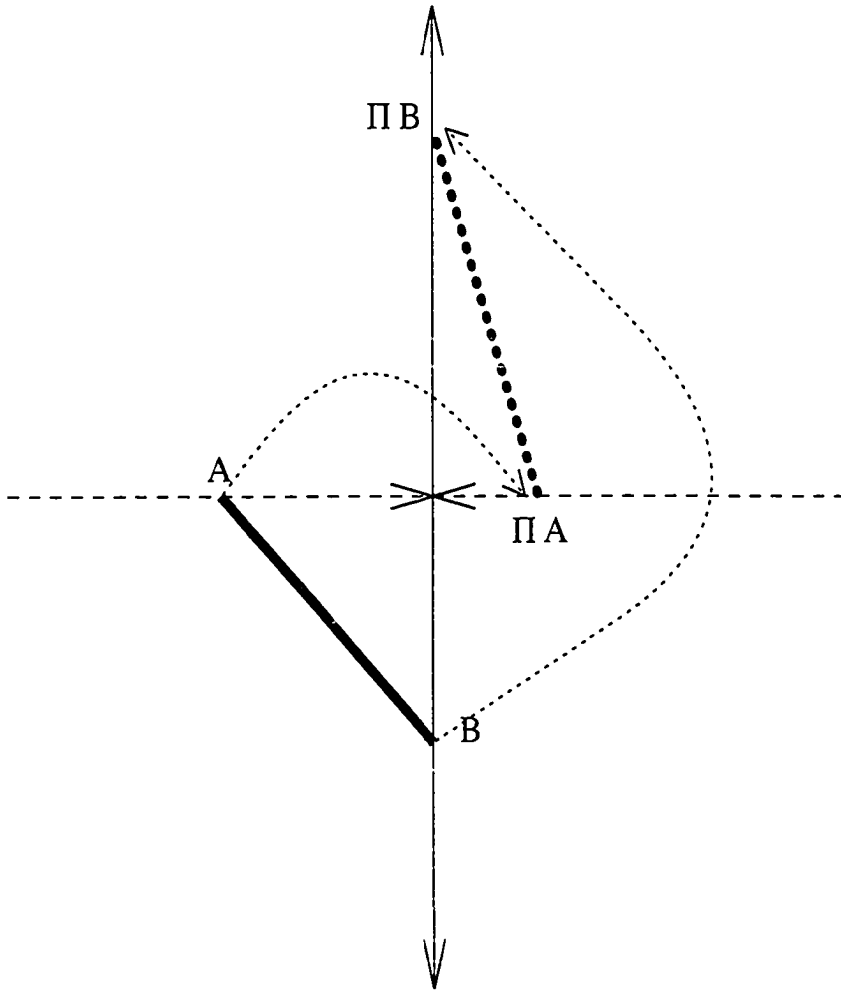


Figure 3.8: Generic mapping for a saddle type linear map with two negative eigenvalues.

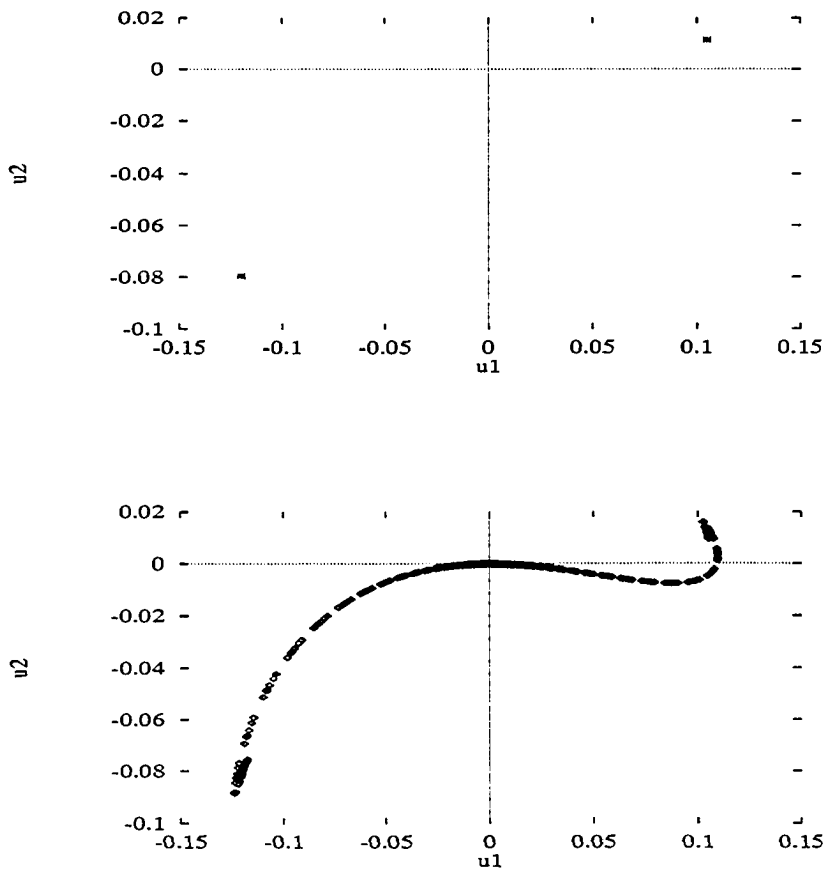


Figure 3.9: Double period fixed points (top) and outflowing manifolds (bottom) in  $u$  coordinates for  $\omega = 2\pi/12,500(\text{yr}^{-1})$  and  $\delta/B = 0.0076$ .

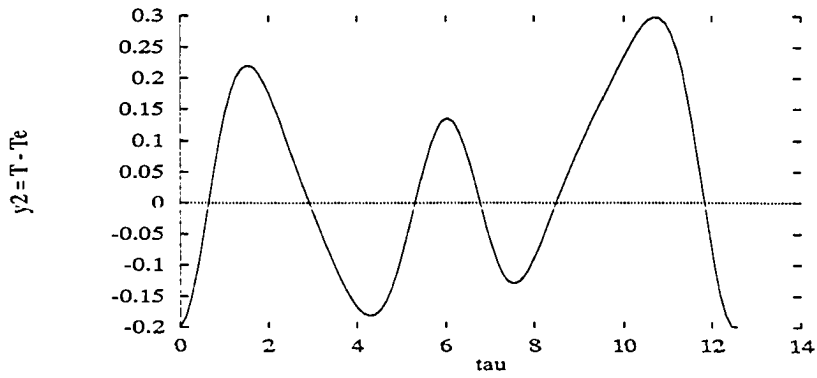
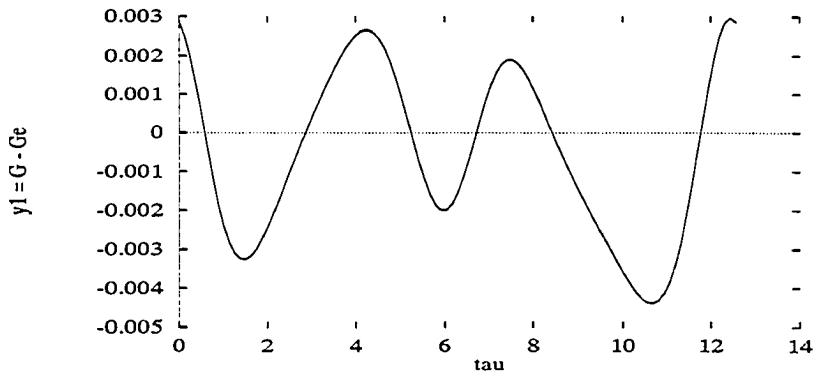


Figure 3.10: Double period wave forms in  $y$  coordinates for  $\omega = 2\pi/12,500(\text{yr}^{-1})$  and  $\delta/B = 0.0076$ .

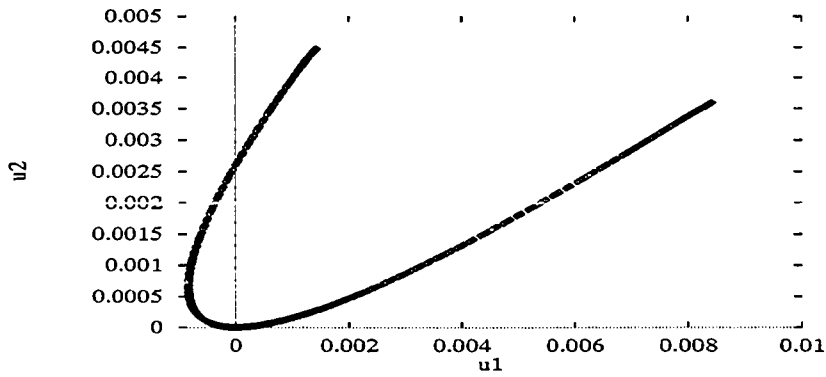
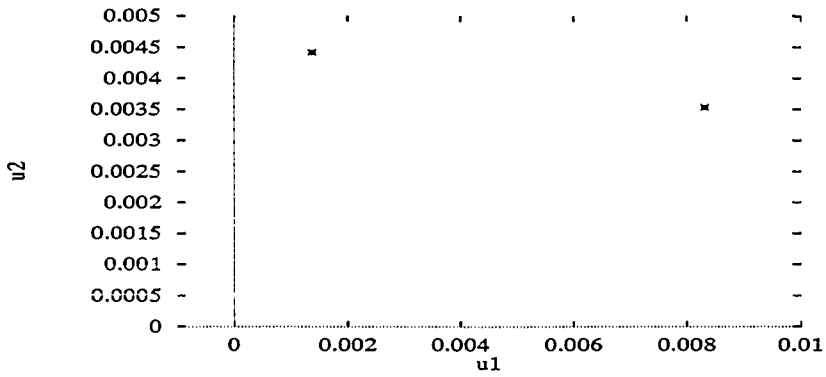


Figure 3.11: Double period fixed points (top) and outflowing manifolds (bottom) in  $\mathbf{u}$  coordinates for  $\omega = 2\pi/26,666(\text{yr}^{-1})$  and  $\delta/B = 0.00272$ .

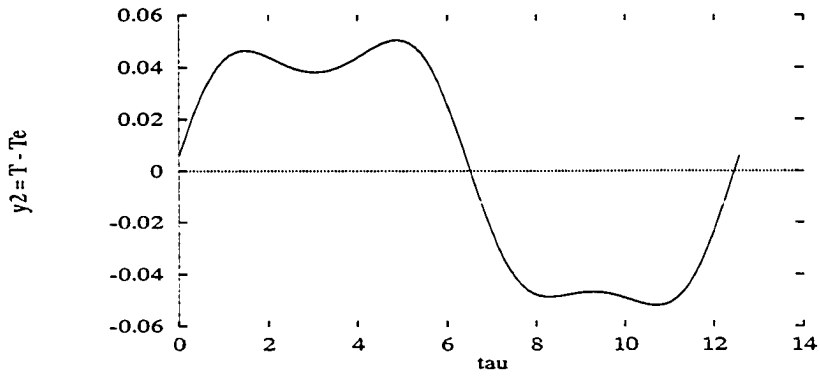
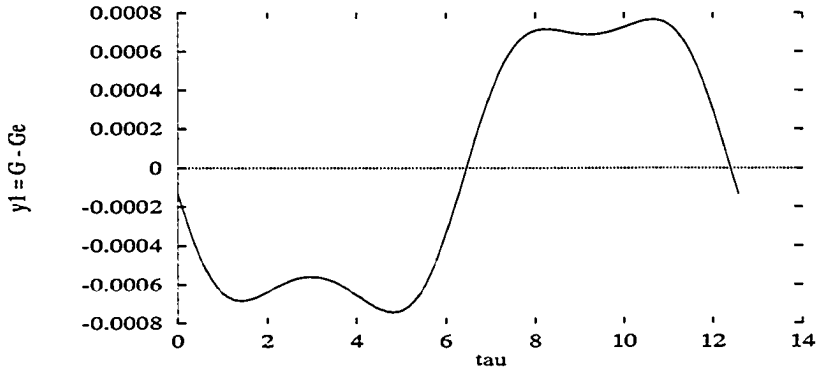


Figure 3.12: Double period wave forms in  $y$  coordinates for  $\omega = 2\pi/26,666(\text{yr}^{-1})$  and  $\delta/B = 0.00272$ .

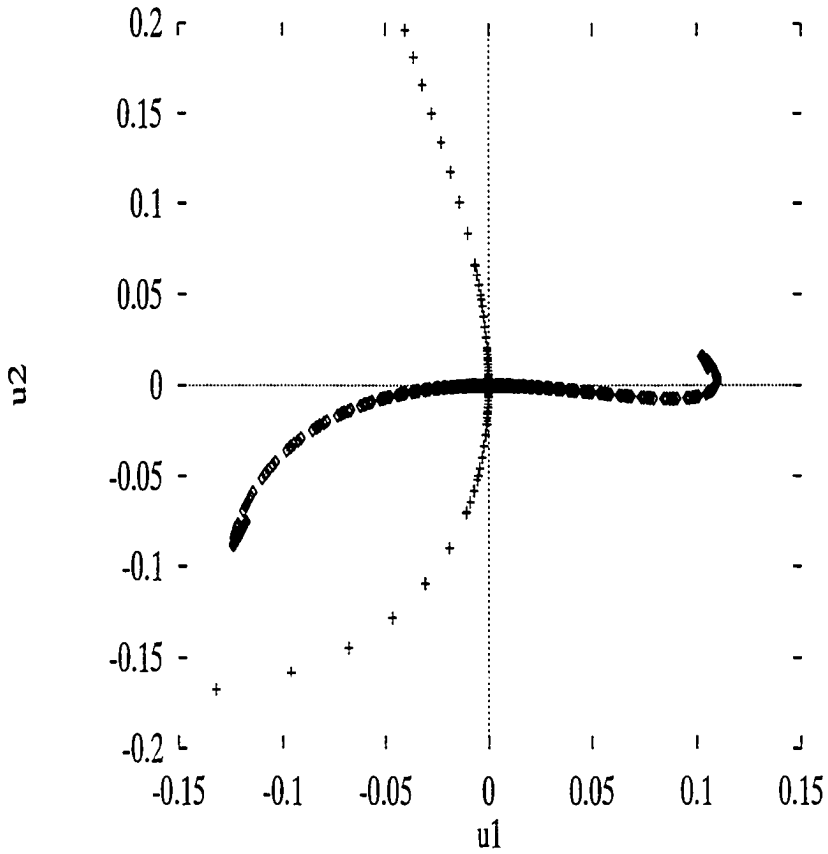


Figure 3.13: Inflowing and outflowing manifolds for the nonchaotic parameters  $\omega = 2\pi/12,500(\text{yr}^{-1})$  and  $\delta/B = 0.0076$ .

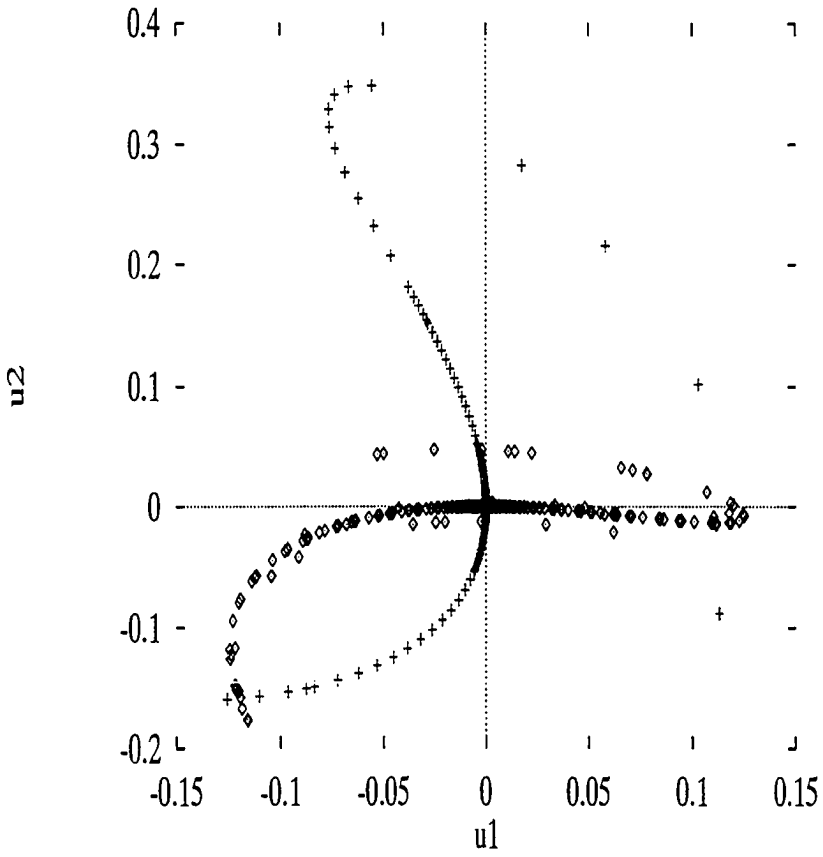


Figure 3.14: Inflowing and outflowing manifolds for the chaotic parameters  $\omega = 2\pi/12,500(\text{yr}^{-1})$  and  $\delta/B = 0.0084$ .

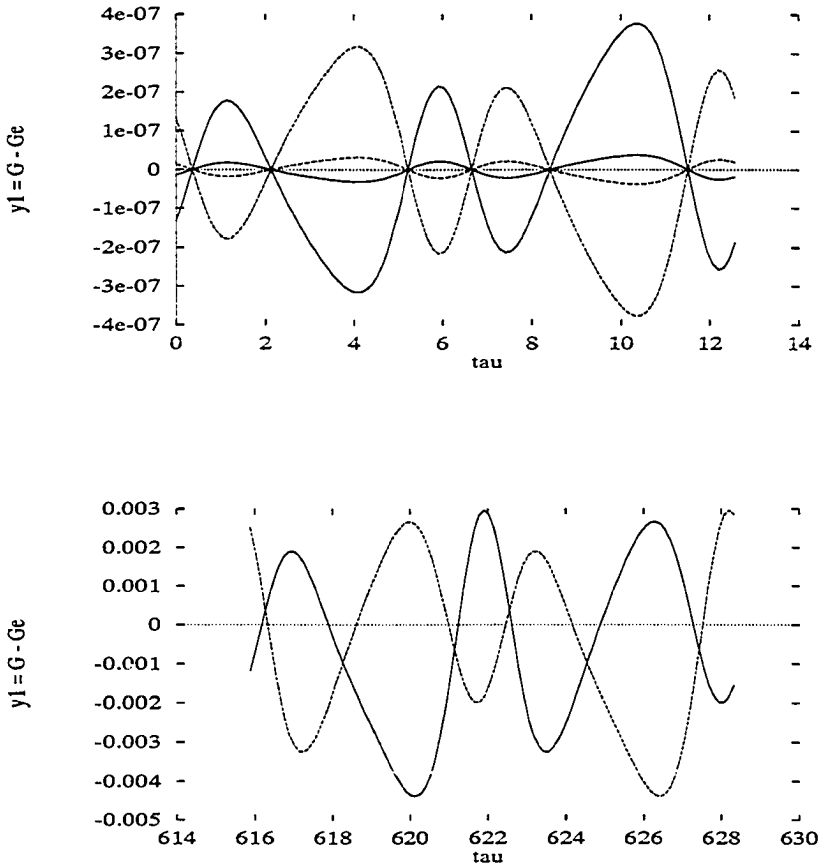


Figure 3.15: Time series for  $y_1 = G - G_e$  of four initial conditions along unstable manifold for the nonchaotic parameters  $\omega = 2\pi/12,500(\text{yr}^{-1})$  and  $\delta/B = 0.0076$ . The two solutions initially in phase (top) on either side of the equilibrium coalesce (bottom) after 100 iterations of the Poincaré map.

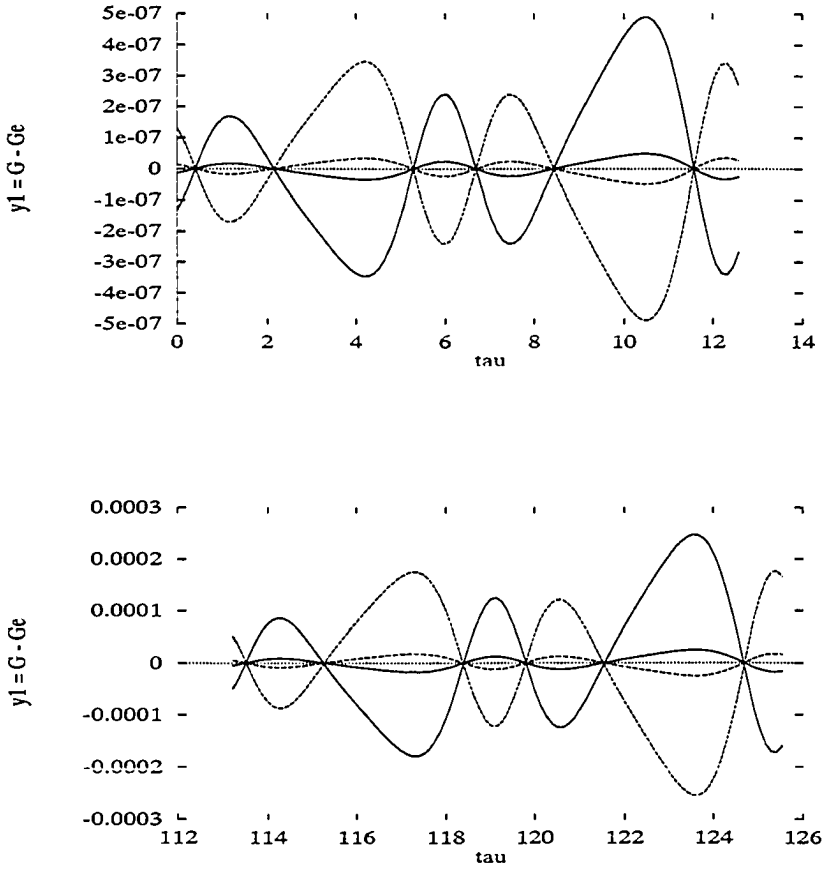


Figure 3.16: Time series for  $y_1 = G - G_e$  of four initial conditions along unstable manifold for the chaotic parameters  $\omega = 2\pi/12,500(\text{yr}^{-1})$  and  $\delta/B = 0.0084$ . The two solutions initially in phase (top) on either side of the equilibrium remain in phase (bottom) after 20 iterations of the Poincaré map.

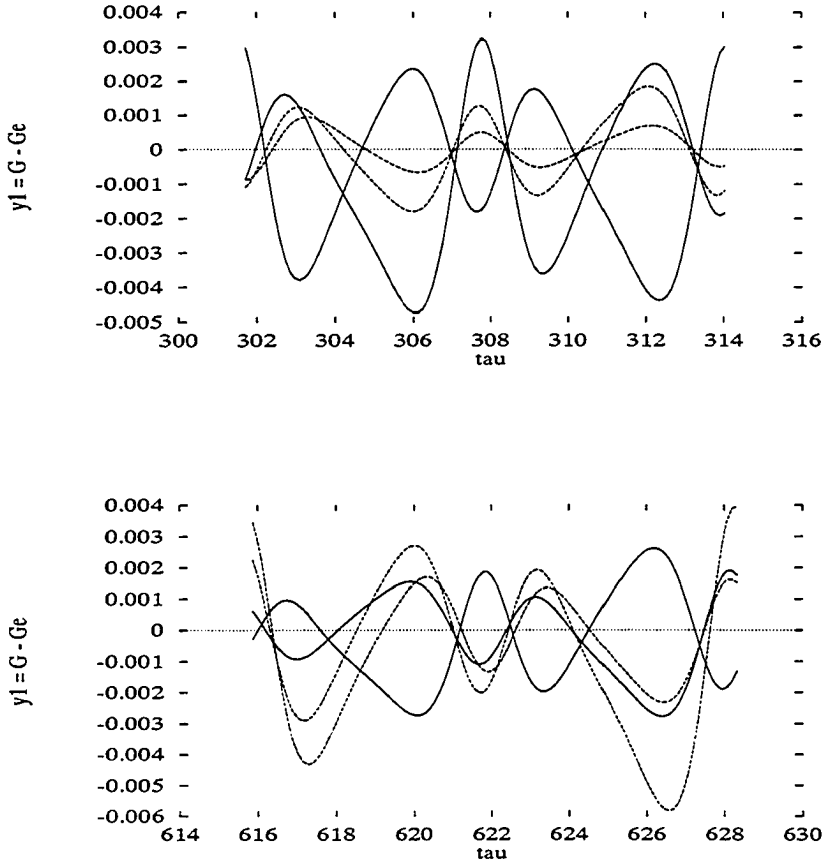


Figure 3.17: Time series for  $y_1 = G - G_e$  of four initial conditions along unstable manifold for the chaotic parameters  $\omega = 2\pi/12,500(\text{yr}^{-1})$  and  $\delta/B = 0.0084$  after 50 iterations (top) and 100 iterations (bottom) of the Poincaré map.

# Chapter 4

## Conclusions

The original question considered was the following: How can frequencies present in ice core data and absent from astronomical variations be generated by the planet internally with global scale thermodynamics? Attempting an answer, we studied an ideal set of physical processes that could describe the interaction of glacier growth with temperature fluctuations. These processes took the form of two nonlinear differential equations. We examined two types of dynamics that give structurally stable periodic motion.

First, orbital variation was neglected. Self sustained oscillation of the internal dynamics about a constant unstable equilibrium was introduced using Poincaré-Andronov-Hopf bifurcation, a well established technique. An analytic expression of the stability constant showed that below a maximum frequency, these oscillations are stable.

The resulting local phase topology involving the second saddle equilibrium, how-

ever, gives a more complete picture of the dynamics. Although not foreseen, the inflowing manifolds of the saddle gave a region of attraction for the periodic orbit. Also not foreseen was the heteroclinic connection to the periodic orbit along an outflowing manifold of the saddle and the resulting homoclinic orbit bifurcating from this connection. This homoclinic orbit occurred when the radius of the self sustained oscillation was fixed and the frequency was lowered, causing the saddle equilibrium to intersect the periodic orbit.

Second, the impact of periodic orbital variation on a stable equilibrium climate was examined. Without relying on the physics of the self sustained oscillation, a periodic internal response at double the external modulation period occurred through saddle node bifurcation. Physically, if the external modulation were removed, the climate behavior would be damped oscillation at a prescribed internal frequency near the modulation frequency.

Frequencies of damped internal oscillation were identified that produced the necessary double period of the Poincaré map upon bifurcation to a saddle. The location of the double period fixed point of the Poincaré map was at the end of the bounded outflowing manifold.

For one particular period doubling scenario, increased magnitude of external modulation caused the inflowing and the outflowing manifolds of the equilibrium to intersect transversally. Hence, the geometric condition of chaotic dynamics was satisfied.

The two nonlinear terms in the equations, logistic growth of the glacier and black body radiation of the temperature, were crucial for the bounded, structurally stable

invariant manifolds observed. Although the physics described is extremely simple, it was sufficient to produce a wide variety of behavior not available with linear systems. This tends to support the importance of these processes in climate dynamics.

Future work could take two general directions. More detailed analysis of the chaotic dynamics is one direction. Verifying chaotic dynamics with other tools of dynamical systems theory is definitely worth pursuing. Posmentier (personal communication) claimed to calculate positive Liapunov exponents, although exact values were not given. Studying these exponents would give an idea of how chaotic the system is and give an indication of the time when solutions separate. The dimension of the attractor could also be calculated to see if it is fractal.

Adding more realistic features to the model is the other direction future work could take. These features could include more albedo variations, temperature effects on vegetation, and more realistic orbital variation. Comparing the model output to ice core data would be useful for simulation of the climate.

Since chaotic dynamics seem to occur with this model, it is very plausible that more realistic models could exhibit similar behavior. The work done here emphasizes the importance of nonlinear dynamics in climate modelling. Techniques used in the analysis of this model are applicable to larger systems of differential equations, although technical complications arise.

# Bibliography

- [1] Roberto Benzi, Giorgio Parisi, Alfonso Sutera, and Angelo Vulpiani. Stochastic resonance in climate change. *Tellus*, 34:10–16, 1982.
- [2] Shui-Nee Chow and Jack K. Hale. *Methods of Bifurcation Theory*. Springer-Verlag, New York, 1982.
- [3] Nikolay P. Erugin. *Linear Systems of Ordinary Differential Equations*. Academic Press, New York, 1966.
- [4] M. Ghil. Climate sensitivity, energy balance models, and oscillatory climate models. *Journal of Geophysical Research*, 89(D1):1280–1284, 1984.
- [5] Michael Ghil and John Tavantzis. Global hopf bifurcation in a simple climate model. *SIAM Journal of Applied Mathematics*, 43(5):1019–1041, 1983.
- [6] Jack K. Hale. *Ordinary Differential Equations*. Wiley-Interscience, New York, 1969.
- [7] Jack K. Hale and Hüseyin Koçak. *Dynamics and Bifurcations*. Springer-Verlag, New York, 1991.

- [8] John Imbrie and John Z. Imbrie. Modeling the climate response to orbital variations. *Science*, 207:943–953, 1980.
- [9] E. N. Lorenz. Deterministic nonperiodic flow. *Journal of the Atmospheric Sciences*, 20:130–141, 1963.
- [10] M. M. Milankovitch. *Cannon of Insolation and the Ice Age Problem*. U. S. Department of Commerce and the National Science Foundation, Washington D. C., 1941.
- [11] J. M. Nese, J. A. Dutton, and R. Wells. Calculated attractor dimensions for low order spectral models. *Journal of the Atmospheric Sciences*, 44:1950–1972, 1987.
- [12] C. Nicolis and G. Nicolis. Stochastic aspects of climate transitions - additive fluctuations. *Tellus*, 33:225–234, 1981.
- [13] Gerald R. North. Analytical solution to a simple climate model with diffusive heat transport. *Journal of the Atmospheric Sciences*, 32:1301–1307, 1975.
- [14] Eric S. Posmentier. Periodic, quasiperiodic, and chaotic behavior in a toy climate model. *Annales Geophysicae*, 8(11):781–790, 1990.
- [15] M. Toner and A. D. Kirwan Jr. Periodic and homoclinic orbits in a toy climate model. *Nonlinear Processes in Geophysics*, 1(1):31–40, 1994.
- [16] S. Wiggins. *Global Bifurcations and Chaos, Analytical Methods*. Springer-Verlag, New York, 1988.

- [17] S. Wiggins. *Introduction to Applied Nonlinear Dynamical Systems and Chaos*.  
Springer-Verlag, New York, 1990.

# Appendix A

## Chosen Equilibrium

The simplest solutions of (1.2.1) are values of  $G$  and  $T$  where  $\dot{G} = \dot{T} = 0$ . While physically rather uninteresting, equilibrium solutions provide a mathematical template of phase flow. Locating such points and determining the stability of each provides neighborhoods in phase space where solutions have predictable behavior. In this section we choose an equilibrium with the soft parameter  $C$  in (1.2.1).

To locate constant equilibrium solutions we observe that (1.2.1) may be written

as

$$\begin{bmatrix} 1 & 0 \\ -L & 1 \end{bmatrix} \begin{bmatrix} \dot{G} \\ \dot{T} \end{bmatrix} = \begin{bmatrix} RG(1-G) - AG - BT + C \\ -KT^4 + F(1-G) \end{bmatrix}. \quad (\text{A.1})$$

One root of the right hand side of (A.1) may be chosen using the constant  $C$  as follows. First substitute

$$G = 1 - \kappa T^4 \quad (\text{A.2})$$

where we have written

$$K = \kappa F \quad (\text{A.3})$$

for convenience. Then we solve

$$-R\kappa^2 T^8 + (A\kappa + R\kappa)T^4 - BT + C - A = 0. \quad (\text{A.4})$$

We may choose an equilibrium temperature  $T_e$  by setting

$$C = R\kappa^2 T_e^8 - (R\kappa + A\kappa)T_e^4 + BT_e + A \quad (\text{A.5})$$

With this choice of  $C$ , we factor (A.4) to obtain

$$\begin{aligned} (T - T_e) \{ & -R\kappa^2 T^7 - T_e R\kappa^2 T^6 - T_e^2 R\kappa^2 T^5 \\ & - T_e^3 R\kappa^2 T^4 + \kappa (R - R\kappa T_e^4 + A) T^3 \\ & + T_e \kappa (R - R\kappa T_e^4 + A) T^2 \\ & + T_e^2 \kappa (R - R\kappa T_e^4 + A) T \\ & - R\kappa^2 T_e^7 + T_e^3 A\kappa + T_e^3 R\kappa - B \} = 0. \end{aligned} \quad (\text{A.6})$$

Other equilibria must be roots to the above seventh order polynomial which depends, among other parameters, on the chosen equilibrium  $T_e$ . The  $k$  ( $2 \leq k \leq 8$ ) equilibrium solutions of (1.2.1) may be indexed as

$$\begin{bmatrix} G_i \\ T_i \end{bmatrix} - \begin{bmatrix} 1 - \kappa T_i^4 \\ T_i \end{bmatrix} \quad (\text{A.7})$$

where  $T_i$  is a solution of (A.6) for  $i = 1, 2, \dots, k$  and  $T_1 = T_e$ .

Notice that a second distinct equilibrium must exist provided the chosen  $T_e$  is not a double root of (A.4). It turns out for the parameter ranges we select, there is only the second equilibrium solution to consider, so we have  $k = 2$ . The polynomial (A.6) will be examined in Appendix D to locate the other root asymptotically using expansion parameters introduced in Appendix C.

# Appendix B

## Complex Eigenvalues and Normal Form

The eigenvalues of  $\mathbf{A}$  are  $(tr(\mathbf{A}) \pm \sqrt{disc(\mathbf{A})})/2$  where  $disc(\mathbf{A}) = tr(\mathbf{A})^2 - 4det(\mathbf{A})$  is the discriminant,  $tr(\mathbf{A})$  is the trace, and  $det(\mathbf{A})$  is the determinant of the two dimensional matrix  $\mathbf{A}$ . To obtain eigenvalues of the form  $\alpha \pm i\omega$  we write the soft parameters  $A$  and  $B$  in terms of  $\alpha$  and  $\omega$ . Specifically, if we set  $tr(\mathbf{A}) = 2\alpha$  and  $det(\mathbf{A}) = \alpha^2 + \omega^2$  then we have the following system

$$\begin{aligned} 2R\kappa T_e^4 - R - A - LB - 4\kappa FT_e^3 &= 2\alpha \\ 4R\kappa FT_e^3 - 8R\kappa^2 T_e^7 F + 4A\kappa FT_e^3 - BF &= \alpha^2 + \omega^2 \end{aligned} \quad (\text{B.1})$$

which may be solved to obtain

$$B = -\frac{16\kappa^2 F^2 T_e^6 + 8\kappa FT_e^3 \alpha + \alpha^2 + \omega^2}{F(1 + 4\kappa T_e^3 L)}$$

$$\begin{aligned}
A &= \frac{1}{F(1+4\kappa T_e^3 L)} \\
&\quad \left\{ 2R\kappa T_e^4 F + 8R\kappa^2 T_e^7 FL - RF - 4RF\kappa T_e^3 L \right. \\
&\quad \left. - 4\kappa F^2 T_e^3 - 2F\alpha + L(\alpha^2 + \omega^2) \right\}. \tag{B.2}
\end{aligned}$$

When (B.2) is put into (1.2.5) the system (1.2.4) will behave as desired. When this is done, we get

$$\begin{aligned}
\mathbf{A}(\alpha, \omega) &= \frac{1}{F(1+4L\kappa T_e^3)} \\
&\quad \left\{ \begin{bmatrix} 4\kappa F^2 T_e^3 & 16\kappa^2 F^2 T_e^6 \\ -F^2 & -4\kappa F^2 T_e^3 \end{bmatrix} \right. \\
&\quad + \alpha \begin{bmatrix} 2F & 8\kappa FT_e^3 \\ 2LF & 8L\kappa FT_e^3 \end{bmatrix} \\
&\quad \left. + (\alpha^2 + \omega^2) \begin{bmatrix} -L & 1 \\ -L^2 & L \end{bmatrix} \right\}. \tag{B.3}
\end{aligned}$$

Note that  $\mathbf{f}(\mathbf{y})$  defined in (1.2.6) remains unchanged since  $A$  and  $B$  are coefficients of exclusively linear terms.

Putting (1.2.4) in a form amenable to analysis, we seek a transformation of the form

$$\mathbf{y} = \mathbf{P}\mathbf{u} \tag{B.4}$$

where  $\mathbf{P}$  is a nonsingular matrix such that

$$\mathbf{P}^{-1} \mathbf{A} \mathbf{P} = \begin{bmatrix} \alpha & \omega \\ -\omega & \alpha \end{bmatrix}. \tag{B.5}$$

To calculate the transformation matrix  $\mathbf{P}$  we determine the eigenvectors of the matrix  $\mathbf{A}$ . Recall that if a matrix has eigenvalues  $\alpha \pm i\omega$ , then the eigenvectors are of the form  $\xi_r \pm i\xi_i$ . Then we form the transformation matrix by setting  $\mathbf{P} = [\xi_r \mid \xi_i]$ .

Having done this, we see that

$$\begin{aligned}
 \mathbf{P} &= \begin{bmatrix} -4\kappa F^2 T_c^3 & 0 \\ F^2 & 0 \end{bmatrix} \\
 &+ \alpha \begin{bmatrix} 4L\kappa F T_c^3 - F & 0 \\ -2LF & 0 \end{bmatrix} \\
 &+ \omega \begin{bmatrix} 0 & -F(1 + 4\kappa T_c^3 L) \\ 0 & 0 \end{bmatrix} \\
 &+ (\alpha^2 + \omega^2) \begin{bmatrix} L & 0 \\ L^2 & 0 \end{bmatrix}. \tag{B.6}
 \end{aligned}$$

# Appendix C

## Poincare-Andronov-Hopf bifurcation

To study the stability of the Poincare-Andronov-Hopf bifurcation we follow the technique outlined in [7]. Let  $\alpha = \lambda\omega$  and consider  $|\lambda| \ll 1$ . Transforming time to  $\tau = \omega t$  the system (1.2.4) with (B.4) becomes

$$\mathbf{u}' = \begin{bmatrix} 0 & 1 \\ -1 & 0 \end{bmatrix} \mathbf{u} + \mathbf{g}(\mathbf{u}) \quad (\text{C.1})$$

where  $(\cdot)' \equiv \frac{d}{d\tau}$  and

$$\mathbf{g}(\mathbf{u}) = \lambda\mathbf{u} + \frac{1}{\omega} \mathbf{P}^{-1} \mathbf{f}(\mathbf{P}\mathbf{u}). \quad (\text{C.2})$$

Now we make the coordinate transformation

$$\mathbf{u} = r \begin{bmatrix} \cos \theta \\ -\sin \theta \end{bmatrix}. \quad (\text{C.3})$$

From the form of  $\begin{bmatrix} r' \\ \theta' \end{bmatrix}$  when (C.3) is used in (C.1), it can be shown that  $\frac{d\theta}{d\tau} > 0$  in a neighborhood of  $\tau = 0$ . Consequently  $\tau$  may be eliminated to obtain the one dimensional equation

$$\frac{dr}{d\theta} = \lambda r + c_2(\lambda, \theta) r^2 + c_3(\lambda, \theta) r^3 + O(r^4). \quad (\text{C.4})$$

The “Big  $O$ ” notation is slightly abused in that the coefficients of the higher order terms are  $2\pi$  periodic dependent on  $\theta$ .

The coordinate transformation to eliminate the  $\theta$  dependence in the first few terms of (C.4) is of the form

$$r = \rho + b_2(\lambda, \theta) \rho^2 + b_3(\lambda, \theta) \rho^3 \quad (\text{C.5})$$

where  $b_2(\lambda, \theta)$  and  $b_3(\lambda, \theta)$  are chosen to be  $2\pi$  periodic in  $\theta$ . When this transformation is put in (C.4) the resulting differential equation for  $\rho$  is

$$\begin{aligned} \frac{d\rho}{d\theta} &= \lambda \rho + \left( c_2 - \frac{db_2}{d\theta} - \lambda b_2 \right) \rho^2 \\ &+ \left( c_3 + 2b_2 \frac{db_2}{d\theta} - \frac{db_3}{d\theta} - 2\lambda(b_3 + b_2^2) \right) \rho^3 \\ &+ O(\rho^4). \end{aligned} \quad (\text{C.6})$$

By requiring

$$\begin{aligned} \frac{db_2}{d\theta}(\lambda, \theta) &= c_2(\lambda, \theta) - \bar{c}_2(\lambda) \\ \frac{db_3}{d\theta}(\lambda, \theta) &= c_3(\lambda, \theta) + 2b_2(\lambda, \theta) \frac{db_2(\lambda, \theta)}{d\theta} - \bar{c}_3(\lambda) \end{aligned} \quad (\text{C.7})$$

where the constants  $\bar{c}_2(\lambda)$  and  $\bar{c}_3(\lambda)$  represent the “average” of the coefficients  $c_2(\lambda, \theta)$  and  $c_3(\lambda, \theta)$  by

$$\begin{aligned}\bar{c}_2(\lambda) &= \frac{1}{2\pi} \int_0^{2\pi} c_2(\lambda, s) ds \\ \bar{c}_3(\lambda) &= \frac{1}{2\pi} \int_0^{2\pi} \left( c_3(\lambda, s) + 2b_2(\lambda, \theta) \frac{db_2(\lambda, \theta)}{d\theta} \right) ds \\ &= \frac{1}{2\pi} \int_0^{2\pi} c_3(\lambda, s) ds\end{aligned}\tag{C.8}$$

we obtain the desired transformation.

From the symmetry in forming (C.4) from a two dimensional equation,  $\bar{c}_2 = 0$ .

With the transformation (C.5) and the definition (C.7) we obtain

$$\frac{d\rho}{d\theta} = \lambda \rho + (\bar{c}_3 + O(\lambda)) \rho^3 + O(\rho^4).\tag{C.9}$$

We analytically determine  $\bar{c}_3$  to be

$$\begin{aligned}\bar{c}_3 &= \left( \frac{\kappa T_e}{1 + 4L\kappa T_e^3} \right) \left( \frac{L^2\omega^2 + F^2}{2\omega^3} \right) \\ &\quad \left\{ 3L^2 (10L\kappa FT_e^3 + T_e R + F) \omega^4 \right. \\ &\quad + (48L^2 F^2 \kappa^2 T_e^7 R - 72L^2 F^3 \kappa^2 T_e^6 \\ &\quad + 8LF\kappa T_e^5 R^2 - 12LF^2 \kappa T_e^4 R \\ &\quad + 30LF^3 \kappa T_e^3 + 2FT_e^2 R^2 + 3F^3) \omega^2 \\ &\quad \left. + 8\kappa^2 T_e^6 F^3 (2T_e R - 3F) (8LR\kappa T_e^4 \right. \\ &\quad \left. + 2T_e R + 3F) \right\} + O(\lambda).\end{aligned}\tag{C.10}$$

The stability of (C.9) is determined by the sign of  $\bar{c}_3$ . Parameter ranges such that  $\bar{c}_3 < 0$  will give rise to a stable nontrivial periodic orbit about the origin. Letting  $a$

represent the radius of the periodic orbit in  $u$  coordinates, we have the approximate bifurcation curve

$$\lambda(a) = -\bar{c}_3 a^2 + O(a^3) , a \rightarrow 0. \quad (\text{C.11})$$

# Appendix D

## The Second Equilibrium

Since the polynomial (A.4) is of even order and we chose one real root using (A.5), there must exist a second real root. In this section, we find an asymptotic approximation for this second equilibrium. With an analytic approximation for the second equilibrium we may analyze the topological character of the dynamics near this equilibrium. Also, the proximity of this equilibrium with respect to the chosen equilibrium is of interest.

In choosing an expansion parameter, we notice that setting  $\alpha = \omega = 0$  in (B.2) and putting this in (A.6) causes  $T_e$  to be a double root. This can be seen by factoring the resulting polynomial to obtain

$$(T - T_e)^2 \left\{ -R\kappa^2 T^6 - 2R\kappa^2 T_e T^5 - 3R\kappa^2 T_e^2 T^4 \right. \\ \left. - 4R\kappa^2 T_e^3 T^3 - \frac{T_e^3(12LR\kappa T_e^4 + 3RT_e + 4F)\kappa^2}{1 + 4\kappa T_e^3 L} T^2 \right. \\ \left. - \frac{2T_e^4(4LR\kappa T_e^4 + RT_e + 4F)\kappa^2}{1 + 4\kappa T_e^3 L} T \right\}$$

$$-\frac{T_c^5(12F+RT_c+4LR\kappa T_c^4)\kappa^2}{1+4\kappa T_c^3L} \} = 0. \quad (D.1)$$

Clearly with the choice of  $\alpha = \omega = 0$  the Jacobi matrix evaluated at the first equilibrium is singular. However, this does provide us with convenient expansion parameters. We will use the approximate radius of the orbit about the first equilibrium,  $a$ , as an expansion parameter instead of  $\alpha$  so we can relate the expansions to the phase dynamics. The coefficients of  $a$  in the expansion are then approximated for small  $\omega$ .

To obtain an expansion in  $a$  for  $T_2$  in (A.7), we substitute (B.2) in (A.6) using (C.11). Recalling that  $\alpha = \lambda\omega$  and  $\bar{c}_3$  is given from (C.10), we let

$$T_2 = \Gamma_0 + \Gamma_1 a + \Gamma_2 a^2 + O(a^3) \quad (D.2)$$

and see that  $\Gamma_0$  is the root of the seventh order polynomial

$$\begin{aligned} & -R\kappa^2 T^7 - R\kappa^2 T_c T^6 - R\kappa^2 T_c^2 T^5 - R\kappa^2 T_c^3 T^4 \\ & + \frac{\kappa(R\kappa T_c^4 F + 4R\kappa^2 T_c^7 FL + L\omega^2 - 4\kappa F^2 T_c^3)}{F(1+4\kappa T_c^3 L)} T^3 \\ & + \frac{\kappa T_c(R\kappa T_c^4 F + 4R\kappa^2 T_c^7 FL + L\omega^2 - 4\kappa F^2 T_c^3)}{F(1+4\kappa T_c^3 L)} T^2 \\ & + \frac{\kappa T_c^2(R\kappa T_c^4 F + 4R\kappa^2 T_c^7 FL + L\omega^2 - 4\kappa F^2 T_c^3)}{F(1+4\kappa T_c^3 L)} T \\ & + \frac{12\kappa^2 F^2 T_c^6 + \omega^2 + \kappa^2 F T_c^7 R + 4\kappa^3 F T_c^{10} LR + \omega^2 \kappa T_c^3 L}{F(1+4\kappa T_c^3 L)} = 0. \end{aligned} \quad (D.3)$$

Assuming now that

$$\Gamma_0 = \gamma_0 + \gamma_1 \omega + \gamma_2 \omega^2 + O(\omega^3) \quad (D.4)$$

we obtain

$$\begin{aligned}\Gamma_0 &= T_e + \frac{(1 + 4\kappa T_e^3 L)}{8FT_e^5\kappa^2(2RT_e + 8LR\kappa T_e^4 + 3F)}\omega^2 \\ &+ O(\omega^4).\end{aligned}\tag{D.5}$$

Now using (D.5) in (D.2) the terms  $\Gamma_1$  and  $\Gamma_2$  can be found from (A.6) with (B.2), (C.11), and (C.10). With the resultant approximation of  $T_2$ ,  $G_2$  is found using (A.7), and we obtain the approximation for the second equilibrium as

$$\begin{aligned}\mathbf{y}_2 &\equiv \begin{bmatrix} G_2 \\ T_2 \end{bmatrix} - \begin{bmatrix} 1 - \kappa T_e^4 \\ T_e \end{bmatrix} \\ &= \frac{(1+4\kappa T_e^3 L)}{(2RT_e+8LR\kappa T_e^4+3F)} \begin{bmatrix} \frac{-1}{2\kappa T_e^2 F} \\ \frac{1}{8FT_e^5\kappa^2} \end{bmatrix} \omega^2 \\ &+ \frac{3F^4(2RT_e-3F)}{2RT_e+8LR\kappa T_e^4+3F} \begin{bmatrix} -\kappa T_e^2 \\ \frac{1}{4T_e} \end{bmatrix} a^2 \\ &+ \begin{bmatrix} O(\omega^4) + O(\omega^2 a^2) \\ O(\omega^4) + O(\omega^2 a^2) \end{bmatrix}.\end{aligned}\tag{D.6}$$

We may now use the approximation (D.6) to evaluate properties of the linearization of (1.2.1) about the second equilibrium. Instead of re-translating to the origin as in (1.2.2), we take advantage of the form of (D.6) and use the coordinates  $\mathbf{y}$  already in use. This should avoid confusion about which origin is being discussed, as  $\mathbf{y} = \mathbf{0}$  will still be the chosen equilibrium. If we let  $\mathbf{h}(\mathbf{y}) = \mathbf{A}\mathbf{y} + \mathbf{f}(\mathbf{y})$  then the Jacobi matrix of

(1.2.4) is

$$Dh(\mathbf{y}) = \mathbf{A} + \begin{bmatrix} -2Ry_1 & 0 \\ -2LRy_1 & -4\kappa Fy_2^3 - 12\kappa Fy_2^2T_e - 12\kappa Fy_2T_e^2 \end{bmatrix} \quad (\text{D.7})$$

where we use the matrix  $\mathbf{A}$  is defined in (B.3).

Using (D.6), we approximate the discriminant of  $Dh$  to determine the nature of the eigenvalues using the lowest order terms in  $a$  and  $\omega$ . Specifically, we see that

$$\begin{aligned} \text{disc}(Dh(\mathbf{y}_2)) &= 4\omega^2 \\ &- \left( 8(2RT_e - 3F)^2 F^4 \kappa^2 T_e^4 \right) a^2 \\ &+ O(\omega^4) + O(\omega^2 a^2). \end{aligned} \quad (\text{D.8})$$

So we will expect two real eigenvalues for fixed  $\omega$  as  $a \rightarrow 0$ . Forming the rest of the eigenvalues, we have

$$\begin{aligned} \mu_{\pm} &= \pm \omega + \frac{(1+4\kappa T_e^3 L)(2RT_e - 3F)}{4\kappa T_e^3 (2RT_e + 8LR\kappa T_e^4 + 3F)F} \omega^2 \\ &+ O(\omega^4) + O\left(\frac{a^2}{\omega^2}\right). \end{aligned} \quad (\text{D.9})$$

Clearly this equilibrium has a saddle character as one eigenvalue is positive and one is negative. Thus we introduce the notation  $\mathbf{y}_{saddle} \equiv \mathbf{y}_2$ . With an equilibrium of this type, the natural structure of the one dimensional invariant manifold provides borders for the phase flow. These inflowing and outflowing (stable and unstable) manifolds may intersect to form a homoclinic orbit.

Homoclinic orbits for conservative or Hamiltonian systems may be written down exactly when they exist. However this luxury is not available for general systems

and numerical integration becomes the basis for determining the existence of such an orbit. In seeking such an orbit, it is helpful to know the stability properties. From [2] it is shown that if the trace of the matrix  $Dh$  in (D.7) is negative, then the homoclinic orbit, if it exists, is asymptotically stable. Analyzing the trace of (D.7) evaluated at (D.6) we see that

$$\begin{aligned} \text{tr}(Dh(y_{\text{saddle}})) &= \frac{(1+4\kappa T_e^3 L)(2RT_e-3F)}{2\kappa T_e^3(2RT_e+8LR\kappa T_e^4+3F)F}\omega^2 \\ &\quad - \frac{8T_e^7\kappa^3 F^5(2RT_e-3F)(2RT_e+8LR\kappa T_e^4+3F)}{1+4\kappa T_e^3 L} \frac{a^2}{\omega^2} \\ &\quad + O(\omega^4) + O(a^2). \end{aligned} \tag{D.10}$$

Noting that all parameters are positive, it follows that the trace is negative for small  $\omega$  as  $a \rightarrow 0$  if  $T_e < \frac{3F}{2R}$ .

# Appendix E

## Floquet Theory

Consider the following linear system

$$\dot{\mathbf{y}} = \mathbf{A}(\sigma t) \mathbf{y} \quad (\text{E.1})$$

where  $\mathbf{A}(\sigma t)$  has period  $2\pi/\sigma$ . Every fundamental matrix solution of (E.1) has the form

$$\mathbf{Y}(t) = \mathbf{Q}(\sigma t) e^{\mathbf{B}t} \quad (\text{E.2})$$

where  $\mathbf{Q}(\sigma t)$  is a periodic matrix of period  $2\pi/\sigma$  and  $\mathbf{B}$  is a constant matrix. Both  $\mathbf{Q}(\sigma t)$  and  $\mathbf{B}$  are  $2 \times 2$ . See [6] or [3] for details on Floquet theory.

Now an appropriate change of coordinates exists to eliminate the time dependence of (E.1), namely we let

$$\mathbf{y} = \mathbf{Q}(\sigma t) \mathbf{w} \quad (\text{E.3})$$

The dynamics of  $\mathbf{w}$  are then given by

$$\dot{\mathbf{w}} = \mathbf{B} \mathbf{w} \quad (\text{E.4})$$

The Poincare map of the linear equation (E.1) is found from the eigenvalues and eigenvectors of the monodromy matrix

$$\mathbf{M} = e^{\mathbf{B}2\pi/\sigma} \quad (\text{E.5})$$

This matrix is difficult in general to determine analytically and we must rely on numerical computation.

In particular, one can obtain the monodromy matrix by integrating the linear equations over one period,  $2\pi/\sigma$ , with initial conditions

$$\mathbf{y}_1(0) = \begin{bmatrix} 1 \\ 0 \end{bmatrix} \quad (\text{E.6})$$

and

$$\mathbf{y}_2(0) = \begin{bmatrix} 0 \\ 1 \end{bmatrix}. \quad (\text{E.7})$$

The monodromy matrix is then formed by augmenting the resulting solutions at  $t = 2\pi/\sigma$

$$\mathbf{M} = [\mathbf{y}_1(2\pi/\sigma) \mid \mathbf{y}_2(2\pi/\sigma)] \quad (\text{E.8})$$

## Autobiographical Statement

Michael Toner was born on March 16, 1967 in Birmingham, Alabama, moved to Ft. Walton, Florida in 1971, and to Panama City, Florida in 1973 where he lived until 1984. In 1984, Mr. Toner attended Florida Institute of Technology in Melbourne Florida. In 1988, he received a Bachelor of Science degree with high honor in Applied Mathematics and then moved to Norfolk, Virginia to attend Old Dominion University. While at F.I.T., he tutored at the Individualized Learning Center in mathematics, computer science, physics, and chemistry.

Mr. Toner received a Master of Science degree in Computational and Applied Mathematics from Old Dominion University in 1990 and will receive his Doctorate in Computational and Applied Mathematics December, 1994. He began working as a teaching assistant at Old Dominion University in 1988 and has taught courses through 1994.

### Publication :

Periodic and Homoclinic Orbits in a Toy Climate Model, *Nonlinear Processes in Geophysics*, 1(1): 31-40, 1994. Co-author is A. D. Kirwan Jr.

### Presentations :

“Topology of a Chaotic Two-Dimensional Climate Model” and “Parametric Time Dependence and Bifurcation Analysis of a Climate Model” at the *European Geophysical Society Annual Assembly* in Grenoble, France April 28, 1994.

“Invariant Manifolds and Bifurcation Parameters of a Toy Climate Model” at the

*American Geophysical Union Chapman Conference on Fractals, Chaos, and Predictability in Oceanography and Meteorology at Galway, Ireland on September 21, 1993.*